Journal Of Materials Science

Volume No. 13

Issue No. 1

Jan - Apr 2025

ENRICHED PUBLICATIONS PVT.LTD

JE - 18,Gupta Colony, Khirki Extn,
Malviya Nagar, New Delhi - 110017.
E- Mail: info@enrichedpublication.com
Phone :- +91-8877340707

Journal Of Materials Science

Aims and Scope

The Journal of Materials Science is now firmly established as the leading source of primary communication for scientists investigating the structure and properties of all engineering materials. The Journal of Materials Science publishes reviews, full-length papers, and short communications recording original research results on, or techniques for studying the relationship between structure, properties, and uses of materials. The subjects are seen from international and interdisciplinary perspectives covering areas including metals, ceramics, glasses, polymers, electrical materials, composite materials, fibers, nanostructured materials, nanocomposites, and biological and biomedical materials.

Journal Of Materials Science

Journal Of Materials Science

(Volume No. 13, Issue No. 1, Jan - Apr 2025)

Contents

Sr. No.	Articles / Authors Name	Pg. No.
1	Silica Modified with Iron(III) Oxide to Support Gold Catalyst for Low Temperature CO Oxidation - *Xiaodong DAI 1, 2, Yuan YAO 3, Huanrong LIU 1*	1 - 12
2	Octagonal Shaped Metamaterial Absorber Based Energy Harvester - *Fatih Ozkan ALKURT 1, Olcay ALTINTAS 1, Mehmet BAKIR 2, Ahmet TAMER 1, Faruk KARADAG 3, Mehmet BAGMANCI 1, Muharrem KARAASLAN 1 , Emin UNAL 1, Oguzhan AKGOL 1*	13 - 30
3	Effect of De-Ashing Strategies on Pore Structure and Electrochemical Performance of Activated Carbons for Supercapacitors - *Weiwei KANG 1, 2, Guangxu HUANG 1, 3 , Qianhao GENG 1, Wentao HOU 1, Youheng YAO 1, Bing XU 1, Baolin XING 1, 3, Chuanxiang ZHANG 1, 3, 4*	31 - 44
4	Characteristics and Sinterability of Ceria Stabilized Zirconia Nanoparticles Prepared by Chemical Methods - *Jānis GRABIS , Dzidra JANKOVIČA, Ints* ŠT*EINS, Māra LUBĀNE, Inta SĪPOLA*	45 - 54
5	DFT Study on Electronic Interactions of Pt, Pd and Au Atoms with γ-Al2O3 - *Han WEI 1, Wenbo DONG 1 , Jianhua CHEN 2, Yuqiong LI 2, Cuihua ZHAO 3*	55 - 63

Silica Modified with Iron(III) Oxide to Support Gold Catalyst for Low Temperature CO Oxidation

Xiaodong DAI 1, 2 , Yuan YAO 3, Huanrong LIU 1
1 Shengli College, China University of Petroleum, Dongying, Shandong, China, 257061
2 Post-doctoral Working Station of University Science Park, China University of Petroleum, Dongying, Shandong, China, 257000
3 Petrochemical Research Institute, CNPC, Beijing, China, 100195

ABSTRACT

Low-temperature oxidation of CO to CO2 plays a key role in broad application prospects. In order to achieve the lowtemperature oxidation of CO, the gold catalyst was prepared using Fe2O3-modified SiO2 as support. The results showed that CO conversion was enhanced over the modified catalyst. At – 10 °C, CO conversion of 95 % could be achieved. The catalysts were characterized by XRD and TEM, and the results showed that the Fe2O3 was dispersed in the form of amorphous state. Attributed to the Au-Fe2O3 interaction, the modified catalyst exhibited excellent performance for the oxidation of CO.

Keywords: gold catalyst, CO oxidation, SiO2, Fe2O3, interaction.

1. INTRODUCTION

Low-temperature CO oxidation has broad application prospects, such as enclosed CO2 laser, gas sensors, spacecraft and submarine, CO masks, automotive emissions, hydrogen fuel cells and environmental protections. So, catalysts research for CO catalytic oxidation at low temperature have attracted more and more attentions. In 1987, Haruta [1] reported that nano-gold supported on metal oxide shows excellent catalytic oxidation performance at low temperature. After that, nanogold used as catalyst for CO oxidation in lots of applications [2 – 7] was widely reported, and it showed great potential for gold as catalysts. Nowadays, gold catalysts with high activity and low loading have been extensively studied [2 – 7]. Meanwhile, people recognized that the factors affecting gold catalysts activity include gold particle size, support properties, the interaction between support and gold. Among them, the gold particle size is considered to be the key factor [3 – 7]. Gold particle size is mainly decided by the support properties and catalyst preparation methods, and therefore, choosing suitable carrier and preparation methods is important to obtain the gold catalysts with high activity.

SiO2 is widely used as catalyst support because of its good chemical stability, thermal and mechanical stability, and low price. The conventional deposition-precipitation method is a common method to synthesize nano-gold catalysts with hydrogen tetrachloroaurate(III) (HAuCl4·4H2O) as gold precursor, but this method requires that the isoelectric point of support should be higher than 7. Unfortunately, the isoelectric point of SiO2 is about 2, which is not suitable for nano-gold loading by the

deposition precipitation method. When using SiO2 as support, the gold precursor should be Au complexes, and the nano-gold catalyst is synthesized by grafting such complexes on SiO2 surface. Notably, this grafting method is complicated, and these Au complexes are more expensive than HAuCl4·4H2O. So, it is necessary to develop a method to prepare nano-gold catalyst supported on SiO2 with high efficiency.

Recently, Li et al. [8] reported that a mesoporous iron oxide-silica composite with a high silica content was synthesized by hydrothermal method, and another composite with high iron content was obtained by etching part of silica in alkaline solution. Then gold catalysts were loaded onto both composites by a deposition-precipitation method, and used for CO oxidation. Owing to the significant progress in nanosynthesis over the last 20 years, it is possible to synthesize the nanoparticles with uniform size, morphology, and compositions [9]. For example, gold nanoparticles can be easily synthesized in a large scale of about "kilogram" level through the octadecylamine (ODA) method [10]. In our study, commercial SiO2 was used as initial support, and impregnation-calcination method was used to modify SiO2 with Fe2O3. When Fe2O3 content was lower than 10 wt%, it prefers to form amorphous dispersion on SiO2 surface, characterized by XRD. Firstly, gold nanoparticles (4 – 6 nm) were synthesized through octadecylamine method, and then were supported on the modified support of Fe2O3/SiO2, getting highly nano-gold catalyst (Au/Fe2O3/SiO2). The experimental results showed that the strong interactions between gold and amorphously dispersed Fe2O3, presenting excellent CO catalytic oxidation performance at low temperature. When reaction temperature was – 10 °C, the CO conversion reached to 95 %. Experiments at temperature range of – 10 ~ 100 °C, the prepared catalyst could last for 200 hours with stable performance. It could be concluded that the prepared catalyst shows a good catalytic activity and stability, and had a promising application prospective.

2. EXPERIMENTAL

2.1. Materials

Urea (NH2CONH2), chloroauric acid tetrahydrate (HAuCl4·4H2O), iron (III) nitrate nonahydrate (Fe (NO3)3·9H2O), and Silica (SiO2) were provided by the national medicine group chemical reagent limited company, and all of them are analytic grade. Au content of the HAuCl4·4H2O is 47.8 wt.%.

2.2. Methods

Iron nitrate (Fe(NO3)3·9H2O) was dissolved in distilled water with certain volume, and then was supported onto SiO2 by the initial immersion method. After ultrasonic treatment for 10 minutes, samples were dried at 100 °C for overnight, and then were calcined at 500 – 600 °C for 5 hours. Finally, catalyst support of Fe2O3/SiO2 was obtained. According to the reported method [10], gold nanoparticles were synthesized and dispersed in cyclohexane. Fe2O3/SiO2 support was impregnated in

cyclohexane solution of gold nanoparticles, and was stirred and evaporated at room temperature to obtain nano-gold catalyst. Catalyst was expressed as Au-x/Fe2O3-y/SiO2 in paper, and "x" and "y" were mass contents of Au and Fe2O3, respectively.

2.3. Characterization

The N2 adsorption/desorption isotherms at – 196 ℃ were obtained using a Autosorb-3B porosity analyzer (Quantachrome USA.). Prior to analysis, samples (0.2 g) were degassed at 400 ℃ for 4 h, until the pressure was less than 1 Pa. The specific surface area was deduced by applying a BET equation from isotherm data. The BJH equation was used to determine the mesopore volume and size distribution. X ray diffraction (XRD) was obtained using D8 type Advance (Bruker company, German), with Cu Kα (λ = 0.154 nm) as radiation source, voltage of 40 kV, current 40 mA, scan rate 0.1 °/min, and scan range 20 – 85°. Surface morphology and particle size of gold nanoparticles were analyzed by transmission electron microscopy (TEM, Japan, JEOL-JEM-2010). Gold content was tested by inductively coupled plasma (ICP-AES) method (Thermo Scient method iCAP 6300 ICP).

2.4. Catalytic testing

0.2 g gold catalyst with 200 – 300 mesh was put into reaction tube (U type), adjusting flow rate of feed gas as required (Fig. 1). Feed gas was consisted of CO with volume content of 1 %, and air of 99 %. Reaction temperature and pressure were set at – 10 – 150 °C and 1.013 × l05 Pa respectively. The gas hourly space velocity (GHSV) of 20000 or 30000 mL g−1 h−1 was used to examine the as-prepared catalysts. Gas chromatography (Shanghai Kechuang chromatograph instrument production company GC9800, N2000 workstation with Zhejiang University Zhida Information Engineering Co. Ltd, Porapak-Q column) was used to measure the content of CO before and after the reaction in the gas mixture.

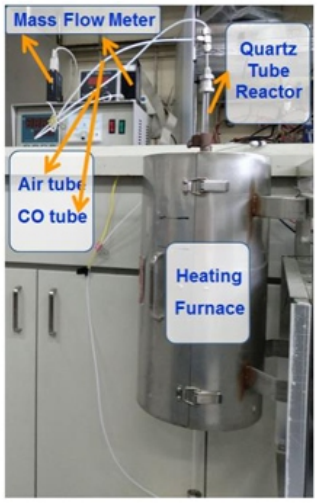

Fig. 1. Experimental set-up for CO oxidation

3. RESULTS AND DISCUSSION

3.1. Synthesis and catalytic performance of pure gold nanoparticles

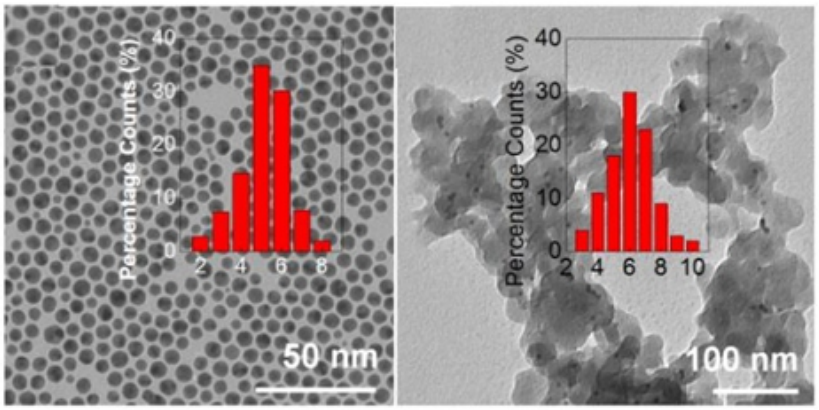

a b

Fig. 2. TEM images: a – of the Au nanoparticles; b – the catalyst Au-3/SiO2

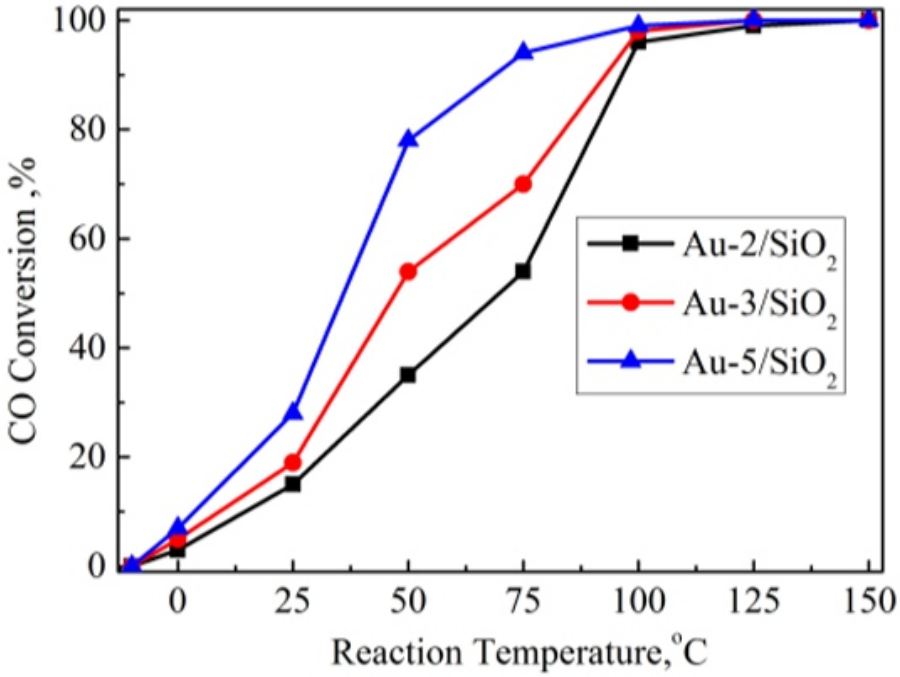

Fig. 3. The performance of the catalyst Au/SiO2 for CO oxidation. GHSV of 20000 mL g−1 h−1

Fig. 2 a shows the TEM image and particle size distribution of the as-synthesized gold nanoparticles [10]. It can be seen that the particle size mainly distributed among 4 – 6 nm. The nano-gold catalyst of Au-3/SiO2 using pristine SiO2 as support is presented in Fig. 2 b with almost unchanged Au size of 5 – 7 nm, and it was tested for the CO oxidation reaction. As indicated in Fig. 3, the Au-3/SiO2 catalyst gave only 20 % CO conversion at 25 °C, which is much lower than the full CO conversion for the reported

gold catalysts under similar conditions [3]. With the increase of gold content, the conversion of CO increased gradually. At 50 °C, the CO conversion was 34 % for the Au-2/SiO2 catalyst, 54 % for the Au-3/SiO2 catalyst, and 78 % for the Au-3/SiO2 catalyst. Obviously, it is difficult to obtain the high CO conversion just via raising the gold content. So, it is necessary to modify the SiO2 support to improve the catalyst performance.

3.2. SiO2 modification with Fe2O3 and its catalytic performance

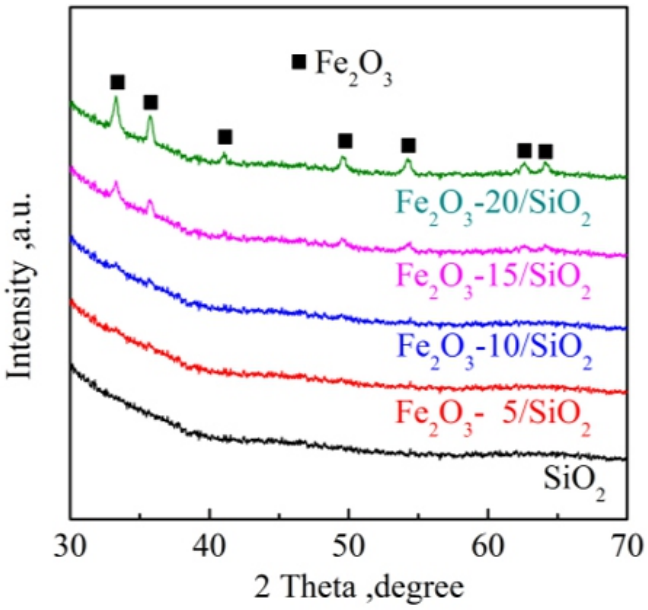

Fig. 4. The XRD patterns of SiO2 and Fe2O3/SiO2 catalysts with different loadings.

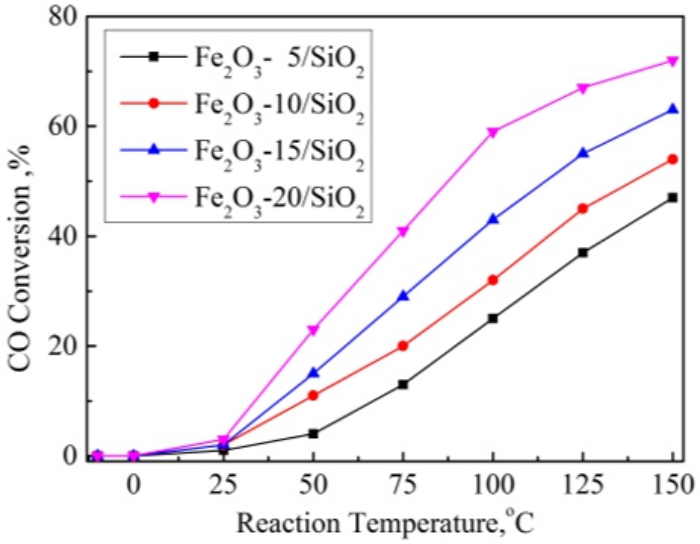

Fig. 5. The performance of the catalyst Fe2O3/SiO2 for CO oxidation. GHSV of 20000 mL g−1 h−1

SiO2 modification with Fe2O3 by impregnationcalcination method was studied in this part. XRD pattern shown in Fig. 4, when Fe2O3 content is lower than 15 wt.%, there is not characteristic peaks of Fe2O3, likely referring to its low weight percentage; while Fe2O3 content is higher than 15 wt.%, the α-Fe2O3 peaks were observed, indicating that crystal structure is formed. This means that the threshold value for Fe2O3 amorphous dispersion is 15 wt.%. Then the catalytic reaction was analyzed, and Fig. 5 shows the performance of the Fe2O3/SiO2 catalyst in CO oxidation. At 50 °C, the Fe2O3/SiO2 sample with 10 wt.% Fe2O3 delivers a CO conversion of 15 %, and when Fe2O3 content increases to 20 wt.%, CO conversion is just increased to 23 %. These results indicated that it is also very difficult to obtain high CO conversion only by increasing Fe2O3 content.

3.3. Preparation of the Au/Fe2O3/SiO2 catalyst and its catalytic performance

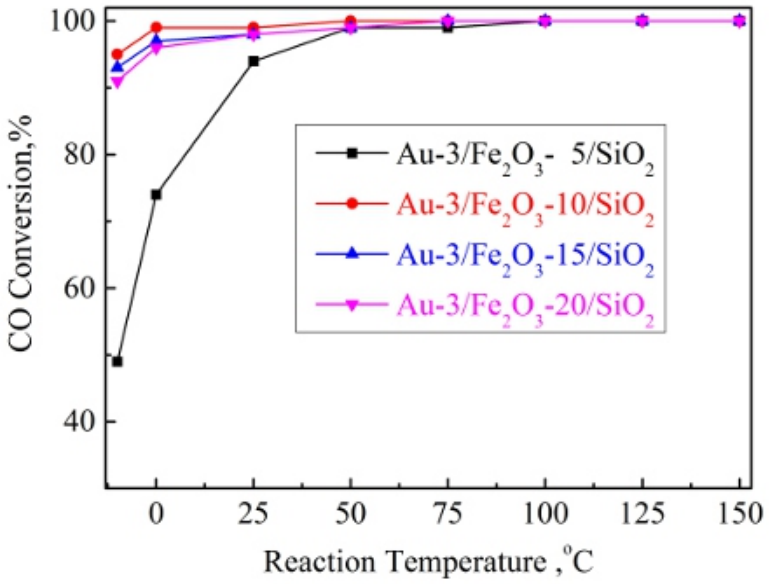

Fig. 6. The influence of Fe2O3 loading on the catalytic performance. GHSV of 20000 mL g−1 h−1

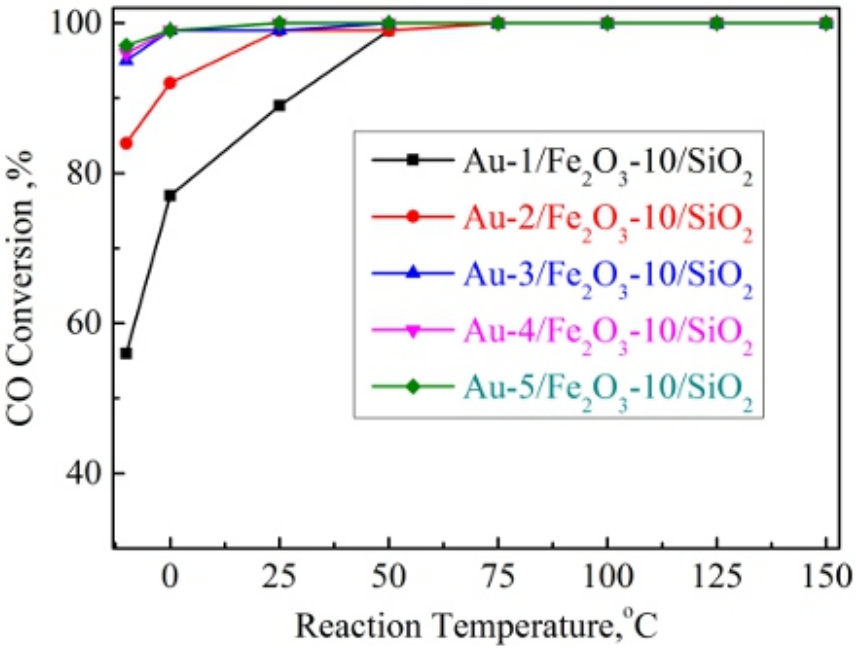

Fig. 6. The influence of gold loading on the catalytic performance. GHSV of 20000 mL g−1 h−1

The catalyst performance of Au/Fe2O3/SiO2 with Au content of 3 wt.% is shown in Fig. 6. At 25 °C, the CO conversion increases to 94 % for the Au-3/Fe2O3-5/SiO2 catalyst (with 5 wt.% Fe2O3 modification), and then increases to 99 % for the Au-3/Fe2O3-10/SiO2 catalyst (with 10 wt.% Fe2O3 modification). After that, with continuous increase of Fe2O3 content to 20 wt.%, the CO conversion is reduced to 94 %. Those results indicate that the Au/Fe2O3/SiO2 catalytic activity is greatly reinforced by adding Fe2O3. In order to optimize the modification conditions, Fe2O3-10/SiO2 was chosen as support to investigate the influence of Au content. It can be observed in Fig. 6 that, at 25 °C, CO conversion gradually grows up from 88 to 99 %, with gold content from 1 to 3 wt.%. After that, with gold content increasing, CO conversion could remain at 99 – 100 %. Through the experiments as above, the best modification conditions can be determined to be 10 wt.% Fe2O3 and 3 – 5 wt.% gold. Also, catalyst stability of Au-3/Fe2O3-10/SiO2 was investigated at the GHSV of 20000 and 30000 mL g−1 h−1, and illustrated in Fig. 7.

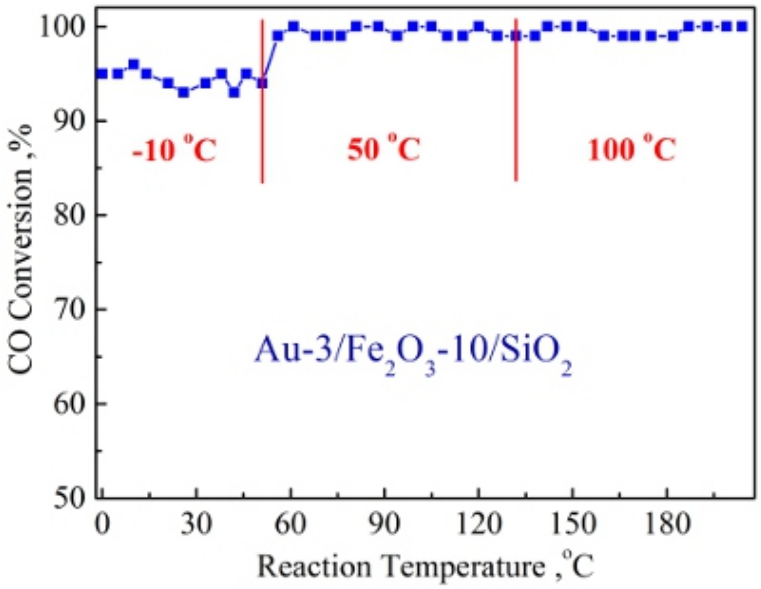

Fig. 7. The stability testing of the Au-3/Fe2O3-10/SiO2 catalyst. GHSV of 20000 and 30000 mL g−1 h−1

When reaction temperature was – 10 °C and at 20000 mL g−1 h−1, CO conversion would stabilize around 93 – 96 % for 50 h. Then, to investigate the high temperature stability of the as-synthesized catalyst, reaction temperature rises to 50 °C and 100 °C, respectively, and both CO conversions could stay at 99 – 100 % for 75 h. Particularly, according to the reported method [11], the GHSV is further increased to 30000 mL g−1 h−1, and the CO conversion at 50 °C could be stably maintained at 91 – 93 % for at least 50 h, which indicates good stability for the Fe2O3 modified gold catalyst. Furthermore, the CO oxidation was carried out at – 10 °C over the 250 h tested catalyst for another 50 h, and the CO conversion is in the range of 93 – 95 % even after the 70 h testing at 100 °C, indicating a good recoverability of this catalyst. By comparison, the Fe2O3 modified catalyst Au-3/Fe2O3-10/SiO2 offers much higher catalytic performance for the CO oxidation than the unmodified counterpart of Au/SiO2.

3.4. Catalytic mechanism

It is interesting that Au-3/Fe2O3-10/SiO2 catalyst has so high activity for CO oxidation after Fe2O3-modification. Some studies have reported that the catalyst structure can be changed during the reaction. For example, the homogeneous nanoalloy of PdZnx was induced into the heterostructure of PdZny@(x-y)ZnO in the real methanol reforming process (CH3OH + H2O = 3H2 + CO2) [12] and Co3O4-nanorod supported single-site Pt catalyst was also in situ induced into PtnCom/CoO1-x for the water-gas shift reaction (CO + H2O = H2 + CO2) [13]. Moreover, the reference [14] reported that silver nanoparticles supported on MnO remove into the pores of MnO and are transformed into silver

monatomic chains during the CH2O oxidation reaction, which is the reason of the excellent catalytic performance. Consequently, the silver nanoparticles can't be detected by XRD after CH2O oxidation reaction. We wonder whether the catalyst structure was changed during CO oxidation reaction, which delivers the high CO oxidation activity.

According to the reported method to examine whether the catalyst structure was changed, we also employed XRD to characterize the Au/Fe2O3-10/SiO2 catalysts with gold content of 2 wt.%, 3 wt.%, 4 wt.% and 5 wt.%. Fig. 8 a illustrates that the characteristic peaks of gold did not disappear.

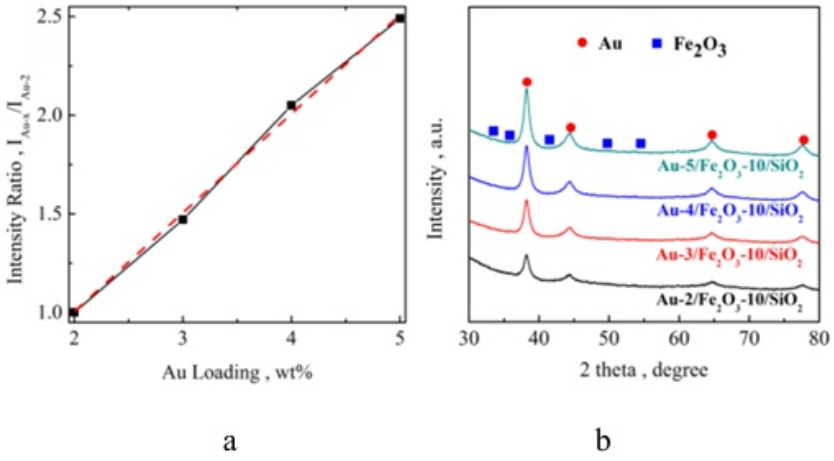

a b

Fig. 8. The XRD patterns: a – of the used b – the intensity ratio of Au(111) over these catalysts: Au2/Fe2O3-10/SiO2;Au-3/Fe2O3-10/SiO2; Au-4/Fe2O310/SiO2; Au-5/Fe2O3-10/SiO2

In order to display this point more clearly, the Au (111) crystal plane intensity was correlated with gold content. If some gold nanoparticles remove into the Fe2O3 and are transformed into gold monatomic chains, the intensity ratios will be different from the ideal intensity ratios. The ideal intensity ratios should be equal to the real gold content ratios for the Au/Fe2O3-10/SiO2 catalysts with gold content of 2 wt.%, 3 wt.%, 4 wt.% and 5 wt.%, which should be 1, 1.5, 2, and 2.5, respectively (with the reference catalyst of Au-2/Fe2O3-10/SiO2). Clearly, the real diffraction intensity ratios of these catalysts are almost equal to their ideal ratios (Fig. 8 b), indicating that the structure of Au nanoparticles did not change during the CO oxidation.

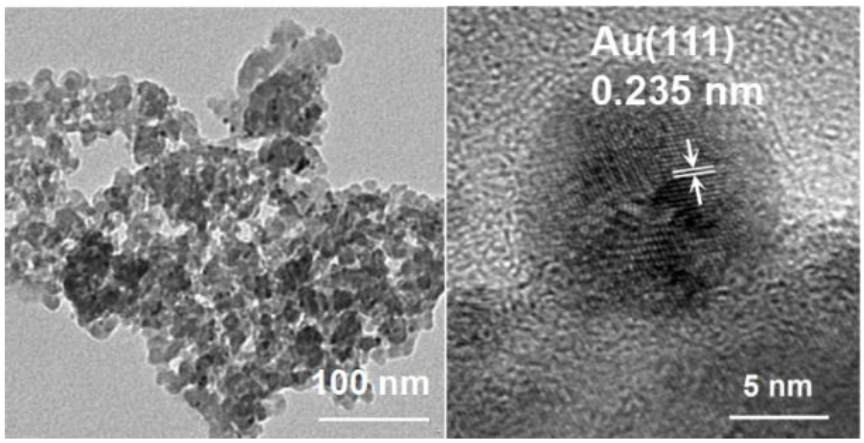

Fig. 9. The images of the used catalyst Au-3/Fe2O3-10/SiO2 : a – TEM ; b – HRTEM

Also, gold particle size was investigated after the reaction. TEM image (Fig. 9 a) shows that the average particle size of gold remains at 5 – 7 nm after reaction, in accordance with gold particle size of the fresh Au/SiO2 in Fig. 1 b, which implies the particle size of gold didn't change in reaction. Lots of results demonstrate that the strong interaction between gold and oxides could promote catalytic performance in oxidation reactions [4]. Fig. 9 b illustrates the lattice fringes of Au particles, and the Au (111) lattice space is 0.235 nm, which is consistent with the reported results [13]. For Fe2O3, its lattice fringe is fuzzy because of its amorphous dispersion. Since the big difference of contrast level between gold and Fe2O3, the close contact of each other is clearly observed in Fig. 9 b. Combining the results in sections 3.1. – 3.3., it is clear that gold and Fe2O3 both had certain catalytic activity for CO oxidation reaction. This is caused by the synergistic effect between gold and Fe2O3, which endows the Au-3/Fe2O310/SiO2 catalyst with excellent catalytic activity. However, the specific synergistic effect mechanism between them should be further investigated, and the works along this line is in progress.

4. CONCLUSIONS

In our study, gold catalyst supported on Fe2O3modified-SiO2 presents very good CO oxidation catalytic performance. When reaction temperature is – 10 ℃, the conversion of CO reaches to 95 %. Fe2O3 is amorphously dispersed when its loading is lower than 10 wt.%, and the catalyst with such Fe2O3 content possesses good catalytic performance attributed to gold and Fe2O3 interface active site. Through Fe2O3 modification to SiO2, it could not only improve the catalytic performance of the catalyst, but also greatly reduce the amount of gold using. In addition, the catalyst shows good stability at different temperatures, which gives good catalyst application prospects.

Acknowledgments

This work was supported by the Scientific Research Starting Fund from Shengli College China University of Petroleum.

REFERENCES

1. Haruta, M., Kobayashi, T., Sano, H., Yamada, N. Novel Gold Catalysts for the Oxidation of Carbon Monoxide at a Temperature far below 0 °C 1987: pp. 405 – 408. https://doi.org/10.1246/cl.1987.405 Chemistry Letters

2 Haruta, M. Size- and Support-dependency in the Catalysis of Gold Catalysis Today 36 1997: pp. 153 – 166. https://doi.org/10.1016/S0920-5861(96)00208-8

3. Bond, G.C., Thompson, D.T. Catalysis by Gold Catalysis Reviews Materials Science and Engineering 1999: pp. 319 – 388. https://doi.org/10.1081/CR-100101171

4. Hashmi, A.S.K., Hutchings, G.J. Gold 41 Catalysis Angewandte Chemie International Edition 2006: pp. 7896 – 7936. https://doi.org/10.1002/anie.200602454 45

5. Min, B.K., Friend, C.M. Heterogeneous Gold-Based Catalysis for Green Chemistry: Low-Temperature CO Oxidation and Propene Oxidation Chemical Reviews 107 2007: pp. 2709 – 2724. https://doi.org/10.1021/cr050954d

6. Pina, C.D., Falletta, E., Prati, L., Rossi, M. Selective Oxidation Using Gold Chemical Society Reviews 2008: pp. 2077 – 2095. https://doi.org/10.1039/B707319B

7. 37 Corma, A., Garcia, H. Supported Gold Nanoparticles as Catalysts for Organic Reactions Chemical Society Reviews 39 2008: pp. 2096 – 2108. https://doi.org/10.1039/B707314N

8. Zhang, W., Lu, X., Zhou, W., Wu, F., Li, J. Mesoporous Iron Oxide-silica Supported Gold Catalysts for Lowtemperature CO Oxidation Chinese Science Bulletin 59 2014: pp. 4008 – 4013. https://doi.org/10.1007/s11434-014-0394-3

9. Liu, Y., Zhao, G., Wang, D., Li, Y. Heterogeneous Catalysis for Green Chemistry Based on Nanocrystals National Science Review 2 2015: pp. 50 – 166. https://doi.org/10.1093/nsr/nwv014

10. Wang, D., Li, Y. Effective Octadecylamine System for Nanocrystal Synthesis Inorganic Chemistry 2011: pp. 5196 – 5202. https://doi.org/10.1021/ic200485v 50

11. Compagnoni, M., Kondrat, S.A., Chan-Thaw, C.E., Morgan, D.J., Wang, D., Prati, L., Villa, A., Dimitratos, N., Rossetti, I. Spectroscopic Investigation of Titania-Supported Gold Nanoparticles Prepared by a Modified Deposition/Precipitation Method for the Oxidation of CO ChemCatChem 8 2016: pp. 2136 – 2145. https://doi.org/10.1002/cctc.201600072

12. Friedrich, M., Penner, S., Heggen, M., Armbrüster, M. High CO2 Selectivity in Methanol Steam Reforming Through ZnPd/ZnO Teamwork Angewandte Chemie International Edition. 52 2013: pp. 4485 – 4488. https://doi.org/10.1002/anie.201209587

13. Zhang, S., Shan, J., Zhu, Y., Frenkel, A.I., Patlolla, A., Huang, W., Yoon, S.J., Wang, L., Yoshida, H., Takeda, S., Tao, F. WGS Catalysis and In Situ Studies of CoO1-x, PtCon/Co3O4, and PtmCom'/CoO1-x Nanorod Catalysts Journal of American Chemical Society 135 8283 – 8293. https://doi.org/10.1021/ja401967y 2013: pp.

14. Huang, Z., Gu, X., Cao, Q. Catalytically Active SingleAtom Sites Fabricated from Silver Particles Angewandte Chemie International Edition 4198 – 4203. https://doi.org/10.1002/anie.201109065 51 2012: pp.

15. Zhou, J., Bo, R.L., Wang, Y. Preparation by DepositionPrecipitation Method of Gold Catalyst for CO Oxidation Fine Chemicals 30 2013: pp. 1117 – 1121. https://doi.org/10.13550/j.jxhg.2013.10.002

Octagonal Shaped Metamaterial Absorber Based Energy

Fatih Ozkan ALKURT 1, Olcay ALTINTAS 1, Mehmet BAKIR 2, Ahmet TAMER 1, Faruk KARADAG 3, Mehmet BAGMANCI 1, Muharrem KARAASLAN 1 , Emin UNAL 1, Oguzhan AKGOL 1

1 Department of Electrical and Electronics Engineering, Iskenderun Technical University,31200, Iskenderun, Hatay, Turkey

2 Department of Computer Engineering, Faculty of Engineering and Architecture, Bozok University, Yozgat, Turkey

3 Department of Physics, Cukurva University, Adana, Turkey

A B S T R A C T

In this study, a novel octagonal shaped metamaterial based broadband absorber is proposed for energy harvesting at WIMAX wireless communication band. The proposal has an absorption of 99.97 % at 5.5 GHz with a bandwidth of 1 GHz between 5 GHz and 6 GHz in Transverse Electric (TE) mode. Transverse Electric (TE), Transverse Magnetic (TM) and Transverse Electromagnetic (TEM) modes are studied numerically in this paper. In TM and TEM modes, proposed structure has absorption of nearly 96 % and 98 % respectively at 6 GHz. The proposed structure is polarization angle independent which is important for energy harvesting applications. Energy harvesting application is realized by using resistive loads on the design, simulations are parametrically studied on resistive loads and experimental study is realized for reflection coefficient measurement and compared with simulated results. Both experimental and simulated results are complying with each other. The proposed structure has different usage areas in stealth areas, detection and imaging.

Keywords: metamaterial absorber, energy harvesting, wireless communication.

1. INTRODUCTION

Metamaterials (MMs) are artificially engineered materials which show specific electromagnetic (EM) properties that cannot be found inherently in the nature. After the proposal of the Victor Veselago in 1967 [1], in 2000, first metamaterial was developed artificially with negative permeability and negative permittivity [2] by using periodic metal resonators. MMs have potential applications in cloaking [3, 4], super lensing [5], antennas [6 – 8], sensors [9 – 12], metamaterial based harvesters and absorbers [13 – 16]. In brief, varied kinds of metamaterials with many applications were analyzed for various applications [17 – 20]. First metamaterial based absorber was introduced by Landy in [15] which is an investigation of unity absorption by using two resonators to captive radiated electromagnetic field. Perfect absorption can be accomplished by arranging the periodic structures in a way that by modification of complex permittivity and permeability for fully absorb electromagnetic energy [21]. Actually, there are several important works in the literature [22 – 25] that is related with perfect

absorption. For example, Bilotti et al. [22] proposed split ring array resonator to absorb microwave energy. Zu et al. [23] suggested that polarization insensitive metamaterial absorber and this study includes fabrication. In another study [24], polarization and incident angle insensitive dualband metamaterial absorber is investigated which is based on isotropic resonators. Cheng and Yang proposed a metamaterial absorber composed of two resonators and a metal wire for increasing the absorption rate in the microwave region in [25]. Yunsong, et al. [26] proposed a subwavelength resolution microwave camera based on a metamaterial absorber and they investigated microwave imaging techniques. In this paper, a novel octagonal shape metamaterial based absorber and energy harvester is designed for Worldwide Interoperability for Microwave Access (WIMAX), wireless communication band with wide band absorption nearly 1 GHz in the resonance region have been proposed. Absorption has been verified by simulation and experimentally and results are compliant with each other. Simulation part of study have been realised by Finite Integration Technique (FIT) based Simulator that supports under Transverse Electric (TE), Transverse Magnetic (TM), and Transverse Electromagnetic (TEM) modes. The proposed structure provides a wide bandwidth and has polarization angle independency.

2. DESIGN AND NUMERICAL SETUP

Design of the proposed structure have been realised by CST Microwave Studio and experimental study results by using parametric and genetic algorithm tools. For the TE and TM mode simulations, boundaries are chosen as unit cell in both X, Y directions and open (add space) in the Z direction. For TEM mode simulation, boundary condition of simulation program has been set to Electric, Magnetic and open add space in simulation. Design details of the proposed structure is given in Fig. 1 a and Table 1. In Fig. 1 b., unit cell of view of the proposed structure is seen. Back side of the proposed design is covered by couple layer to prevent transmission and reduce reflection coefficient level. Proposed structure is placed on FR4 substrate which is 24 mm × 24 mm in X and Y dimensions and it has a thickness of 3.2 mm to increase absorption and bandwidth. Resonator is made up of copper that has a conductivity of 5.8 · 107 S/m and it has a thickness of 0.035 mm.

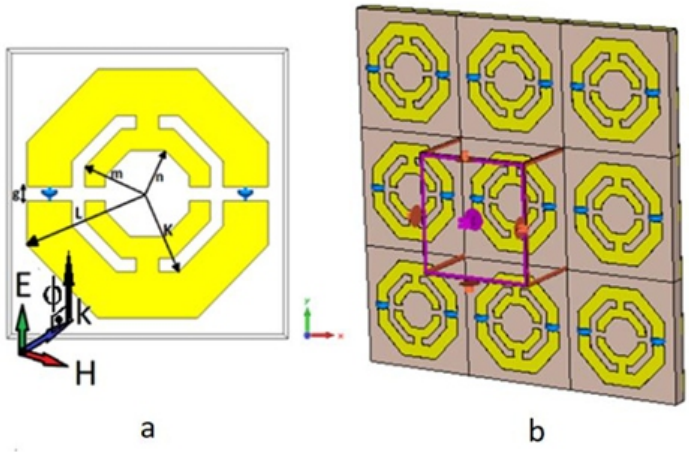

Fig. 1. A novel octagonal metamaterial based absorber design with resistive loads with incident angle phi (ϕ) 90 deg: a – unit cell structure; b – metamaterial full structure

Table 1. Parameters of the proposed structure

Load	K, mm	L, mm	m, mm	n, mm	g, mm
325 ohm	105	7.6	6	4	1.2

The absorption)term can be defined according to equation) = 1)), where R(w) and T(w) indicates reflection and transmission coefficients of the proposed structure. The absorption formula can be minimized by using a metal back plate to prevent transmission, so) = 21|2 = 0. As a result of using metal back plate, absorption formula revised to) = 1 −) = 1− 11|2. From the revised formula, when the reflection is minimum so the absorption will be maximum and transmission coefficient is assumed to be zero in this study. In order to explain design properties of the proposed structure, first of all effect of the resistive load which is used as a lumped element on absorption have been investigated. Absorption versus frequency between 3 GHZ and 7 Ghz when resistor is not used on the structure has been given in Fig. 2. In this usage, simulation results show that the structure has low absorptivity nearly 33 % between 5 Ghz and 6 GHz band in the TE mode.

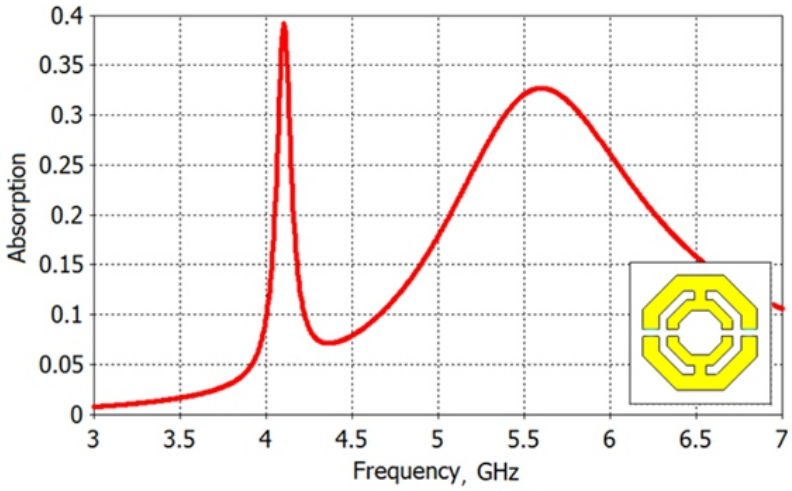

Fig. 2. Absorption of the octagonal metamaterial absorber without resistive loads

In order to find proper resistive load values a parametric study have been realised by simulation program as shown in Fig. 3. According to simulation study results, best bandwidth has been obtained in 325 ohm lumped element resistance value. As shown in Fig. 3, lumped element resistive load values have been analysed between 200 ohm and 1000 ohm values at 10 different values. Since perfect absorption together with desired bands have been supplied when 325 ohm resistive load, this value becomes the design input of the proposed structure.

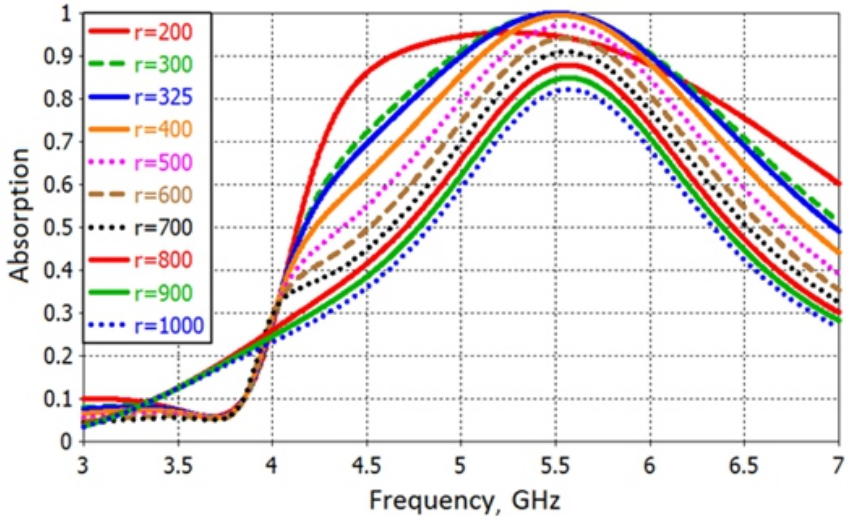

Fig. 3. Parametric study for the resistive load between 200 ohm and 1000 ohm at 6 different points between 3 GHz and 7 Ghz

Another simulation study has been realized to give more information about design parameters of the proposed structure that absorption value according to K and L values of the proposed structure is studied. Obtained simulation results are presented in Fig. 4. and Fig. 5. First of all, L value and resistive

load values have been fixed to 10.5 mm and 325 ohm to see effects of L parameter in absorption. L parameter is now adjusted between 6.8 mm and 8.4 mm in 5 different values as will be presented in Fig. 4.

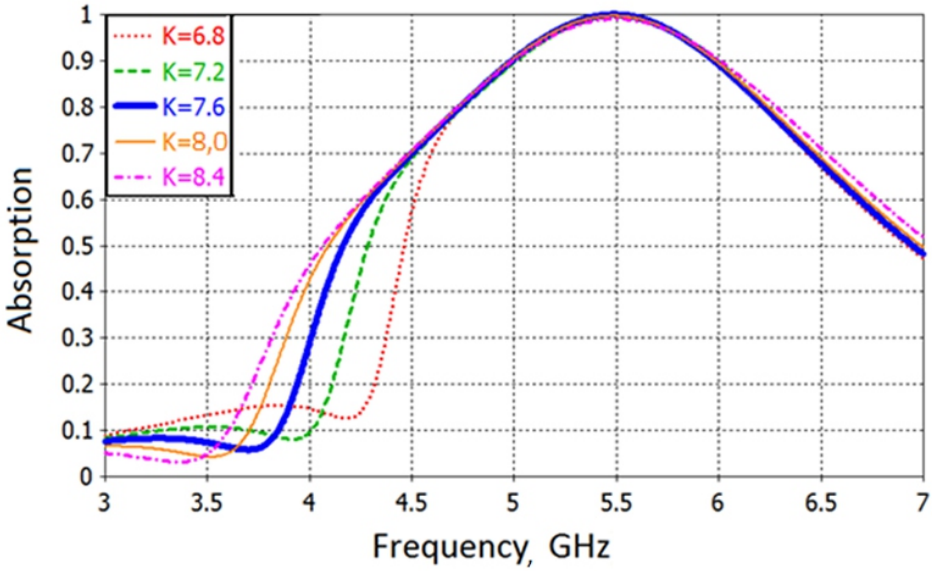

Fig. 4. Parametric result for the K value, L = 10.5 mm, R = 325 ohm

According to simulation study results, K value is decided to be 7.6 mm due to perfect absorption and desired frequency bands. After simulating K parameters, L value in the proposed structure has been shown in Fig. 5. when lumped element resistor value is fixed to 325 ohm and K value is fixed to 7.6 mm. After these pre adjustments, L value is simulated between 9.5 and 11.5 mm in 5 different values and obtained results are given in Fig. 5. As shown in Fig. 5., absorption frequency has been shifted from 4.9 GHz to 6 GHz when L value is increase from 9.5 mm to 11 mm. This value is acting an important role on absorption frequency since 1 mm in change result with 1 GHz shift in the resonance frequency which is good tuning option for changing absorption frequency.

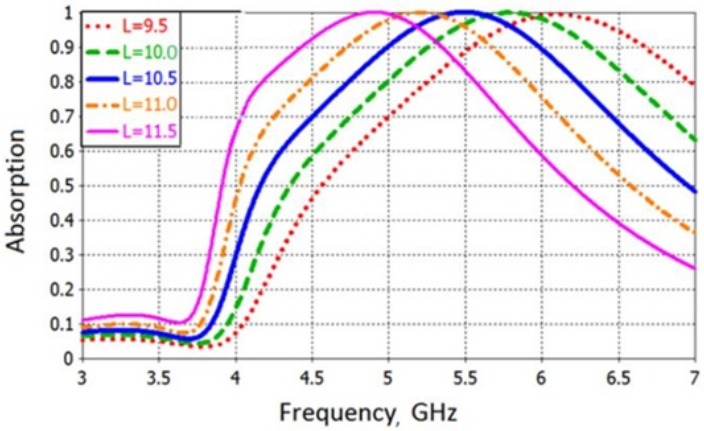

Fig. 5. Parametric result for the L value, K = 7.6 mm, R = 325 ohm

Another parameter has been studied by simulation to give more information about design details that is gap value. In this part of study, resistive loads and the dimensions of outer octagonal ring were chosen as R = 325 ohm, K = 7.6 mm and L = 10.5 mm and gap value is changed between 0.4 mm to 2 mm in the same frequency band. As presented in Fig. 6., gap values have been changed from 0.4 mm to 2 mm and this change in the gap value results with an absorption frequency shift from 5 GHz to 5.7 GHz. After giving information about design details in the proposed structure' usage for WIMAX frequency band operations, In the next section, microwave energy harvesting applications of the proposed structure is discussed.

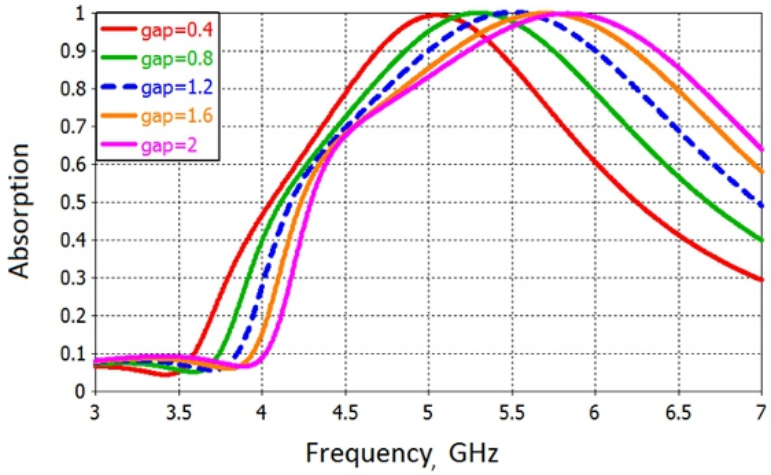

Fig. 6. Parametric results for the gap (mm) with 325 ohm resistive loads

3. TE, TM AND TEM MODE ANALYSIS

In this section, the behavior of the proposed octagonal shape metamaterial absorber is investigated in TE, TM and TEM modes. First of all, S11 value is investigated when TE polarization is applied to the proposed structure. As shown in Fig. 7., wideband perfect absorption is seen between 5 GHz and 6 GHz which is also WIMAX operation frequency. Absorption value increases to 99.97 % value at 5.5 GHz in TE mode. In order to show the absorption properties of the proposed structure in other modes as TM and TEM modes, these modes have been simulated by simulation program and obtained results are given in Fig. 8. As shown in Fig. 8., wideband property of the proposed structure under TEM and TM modes cannot be seen between 3 GHz and 7 Ghz. Single resonance points occur at 6 GHz at 97 % absorption with a bandwidth of 100 Mhz.

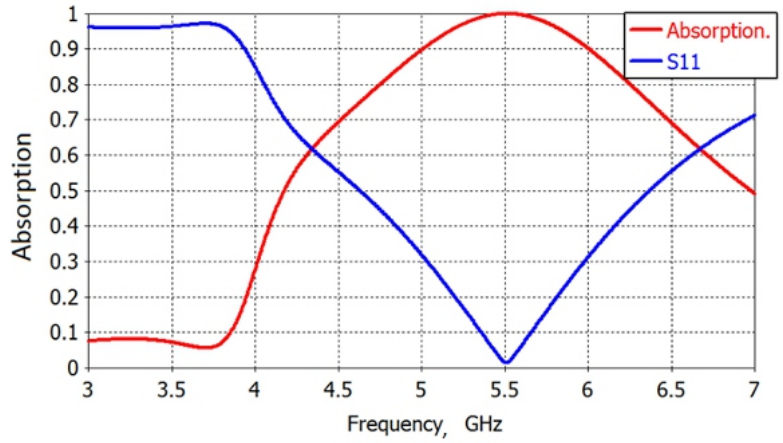

Fig. 7. Absorption and scattering parameter S11 of the proposed structure under TE mode wave

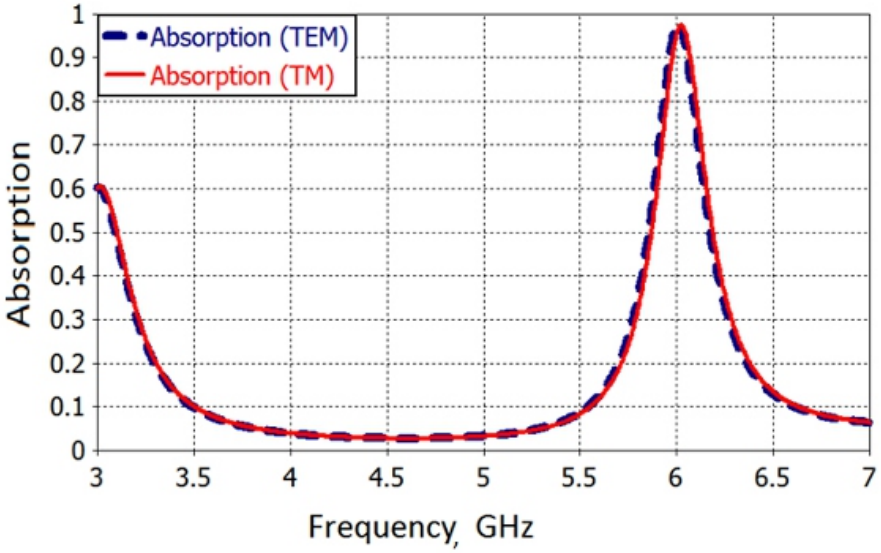

Fig. 8. Absorption of the proposed structure under both TM and TEM modes

Polarization angle independence is another important factor for metamaterial absorber in different polarization angle applications. In order to show the polarization angle effects on absorption, following simulation studies have been realized in TE, TM and TEM mode applications. Obtained results are presented in Fig. 9, Fig. 10 and Fig. 11, respectively.

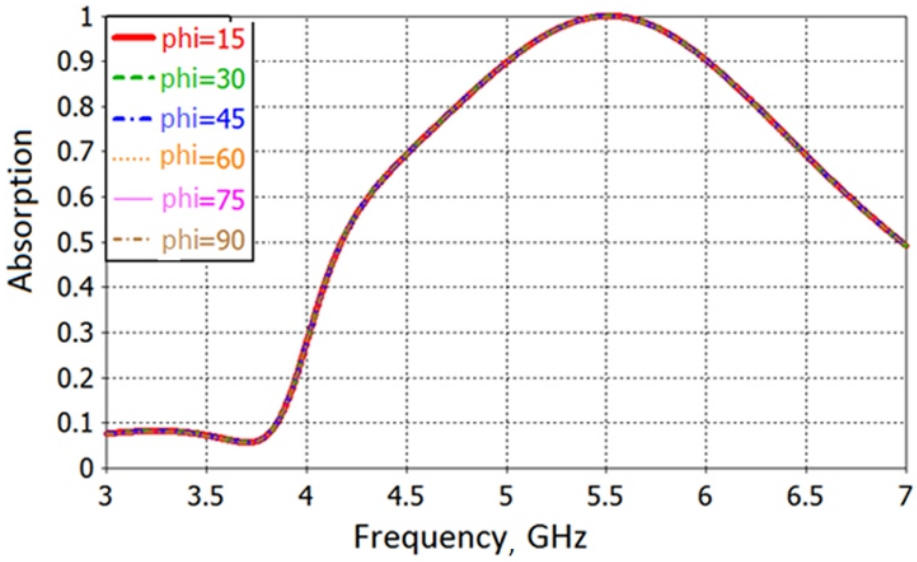

Fig. 9. Absorption under various polarization angle phi for TE mode

When we look at these graphs, we see that phi angle has been adjusted between 0° and 90° in 7 different points and absorption value is simulated between 3 GHz and 7 GHz.These change in phi angle under the TE, TM and TEM mode applications, do not result with a change in absorption that is a wanted situation for absorber studies.According to Fig. 9, Fig. 10 and Fig. 11, it is clear now that the proposed structure, polarization angle independent under TE, TM and TEM modes.

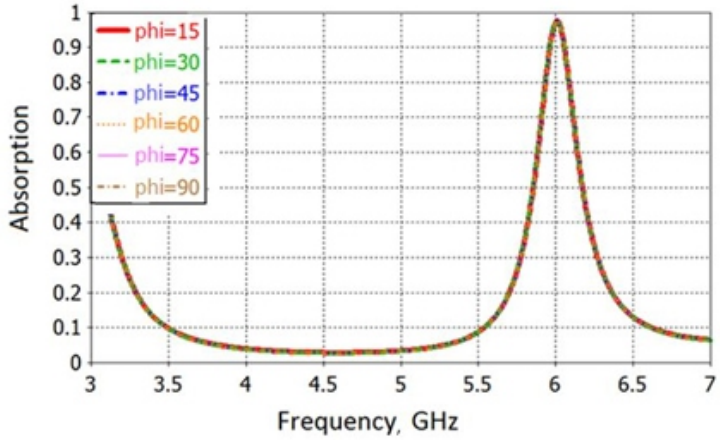

Fig. 10. Absorption under various polarization angle phi for TM mode

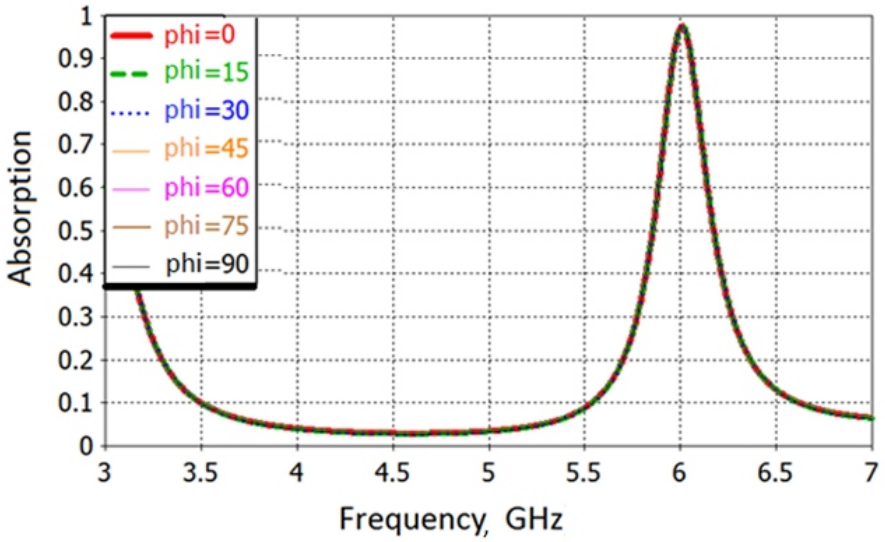

Fig. 11. Absorption under various polarization angle phi for TEM mode

In addition to the polarization angle independency, wide band absorption in TE mode is still protected. These simulation results prove that the proposed structure is a good choice to use in WIMAX frequency portion of microwave spectrum.

4. ELECTRIC FIELD AND SURFACE CURRENT DISTRIBUTIONS

In this part of the study, electric field and surface current distributions have been simulated in TE, TM and TEM mode operations. Obtained results are presented in Fig. 12 and Fig. 13. In Fig. 12, electric field distribution is shown under TE mode at 5.5 GHz which has the maximum absorption nearly 99.97 % absorptivity at that frequency. Then, Fig. 12 b and Fig. 12 c, electric field distributions are shown in TM and TEM modes respectively. All graphics are shown in the same scale (130-190 dB-1uV/m) to see the differences.

When we look at the Fig. 12 a, electric field is concentrated around the splits of the proposed structure which is complying with the direction of electric field electric field is weakening as getting away from centre.

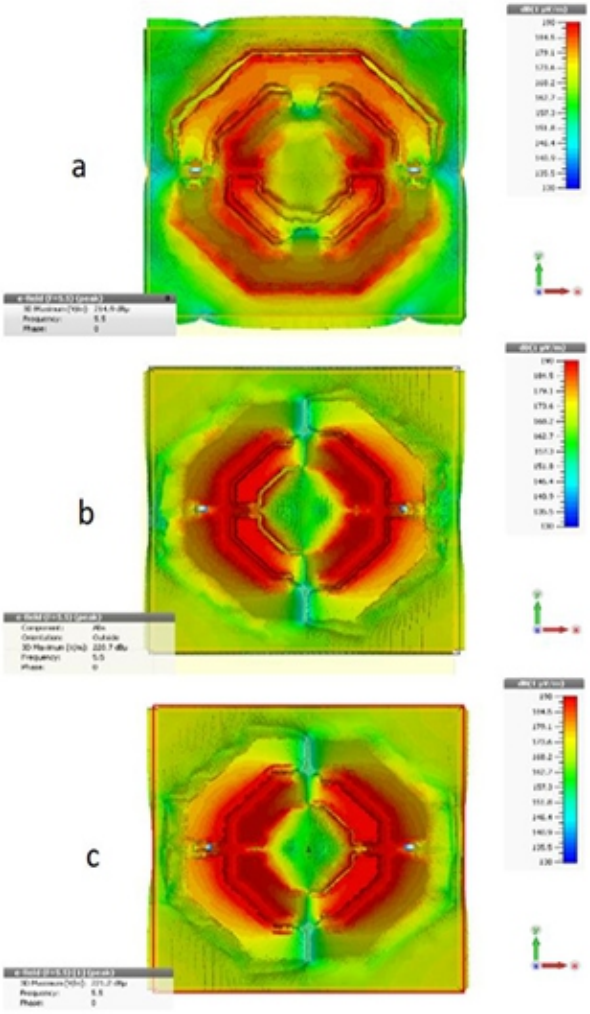

Fig. 12. a – electric field distribution for TE mode; b – electric field distribution for TM mode; c – electric field distribution for TEM mode

In TM and TEM modes, electric field distribution is concentrated at left and right side of the structure according to the dimension of the electric and magnetic field. Surface current distributions of the proposed structure at the resonance frequency of 5.5 GHz, is given in Fig. 13 a,b and c, respectively for TE, TM and TEM mode operations.

The electric field component of incident wave excites free electrons as a surface current, surface charge oscillates along the external electric field and this field causes magnetic dipole moment and the dipole moment creates resonance absorption. As it seen from Fig. 13 a, for TE mode, there are parallel and anti-parallel surface currents on the structure. While parallel currents induce electric field, anti-parallel currents result in magnetic field. These responses couple with E and H components of the incident electromagnetic wave and produces strong localized electromagnetic field at the resonance frequency. Similar simulation results for TM and TEM mode are also obtained with TE mode operations. According to simulated electric and surface current distributions strong magnetic fields can be seen at

the resonance frequencies which is important for energy harvesting applications. In the next sections, energy harvesting performance of the proposed structure and experimental study for reflection coefficient is given.

Resistive elements that have been used as a lumped network element can be used for energy harvesting. For simulation, power on the 325 ohm resistor is chosen as example in TE mode and results are presented in Fig. 14.

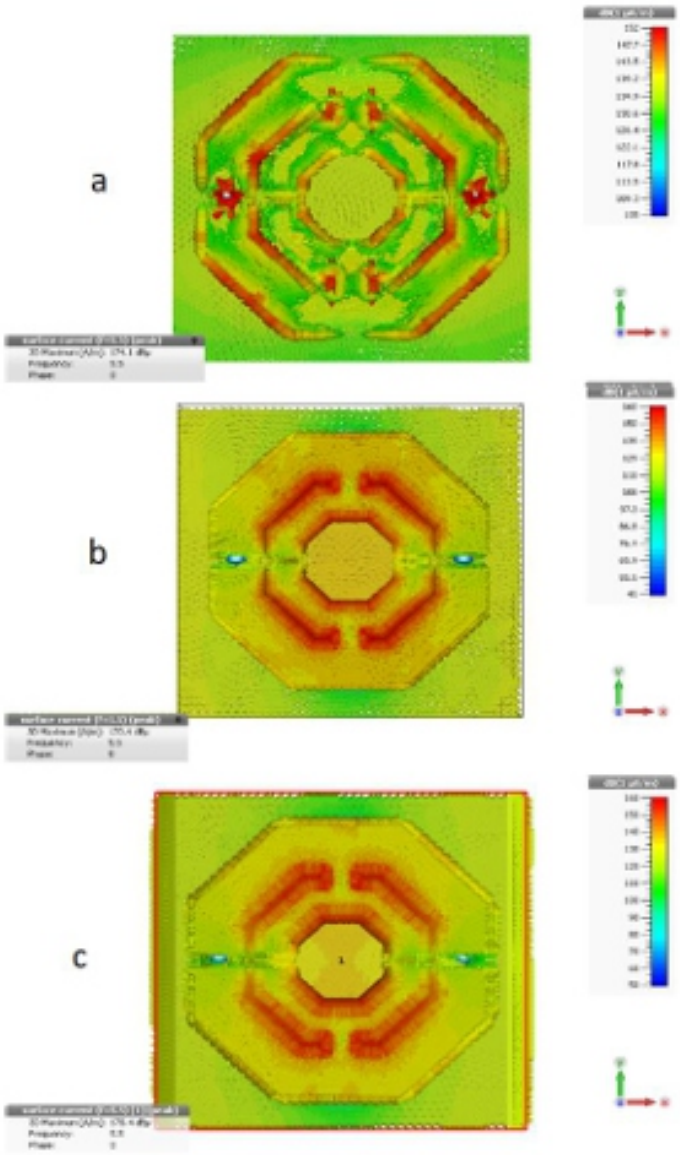

Fig. 13. a – surface current distribution for TE mode; b – surface current distribution for TM mode; c – surface current distribution for TEM mode at 5.5 GHz

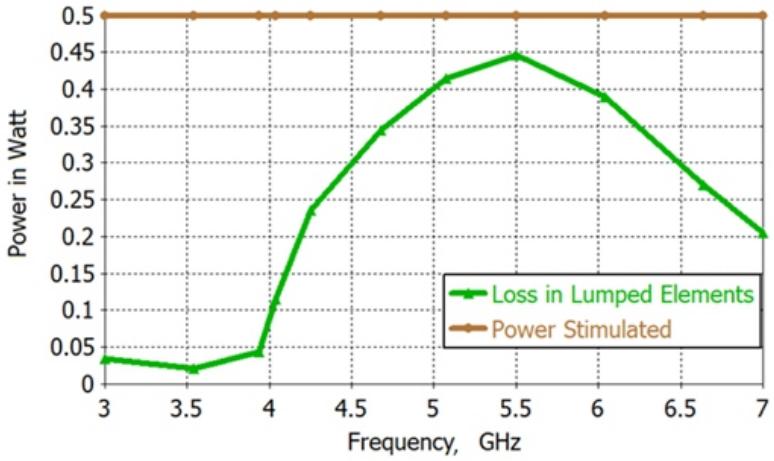

Fig. 14. Simulated power input and energy harvesting efficiency of the proposed structure between 3 and 7 GHz under the

TE mode

As it seen from the figure, while 0.5 W power applied by simulation program between 3 and 7 GHz, 0.45 W of the applied signal is harvested again across the lumped element resistor at the frequency of 5.5 GHz. Simulated energy harvesting efficiency is found as 90 % at the resonance frequency of 5.5 GHz and it is more than 80 % between 5 and 6 GHz. This value decreases to minimum 5 % at 4 Ghz. Thus, the power on the resistive elements can be used in the harvesting system in microwave frequency region such as, WIMAX bands. In addition to the energy harvesting efficiency between 5 and 6 GHz, this values are not affected by polarization change of the applied signal which is also important for energy harvesting applications. In order to support the energy harvesting application of the proposed structure, we have experimentally tested the proposed structure for reflection coefficient measurements. Results of the experimental study can be used for checking the accuracy of the simulations of the proposed octagonal shape metamaterial absorber. The fabricated structure has 49 unit cells in 7 × 7 array shown in the Fig. 15. Promat LPKF E33 CNC controlled PCB production machine is used for the fabrication of the sample which is given in Fig. 15.

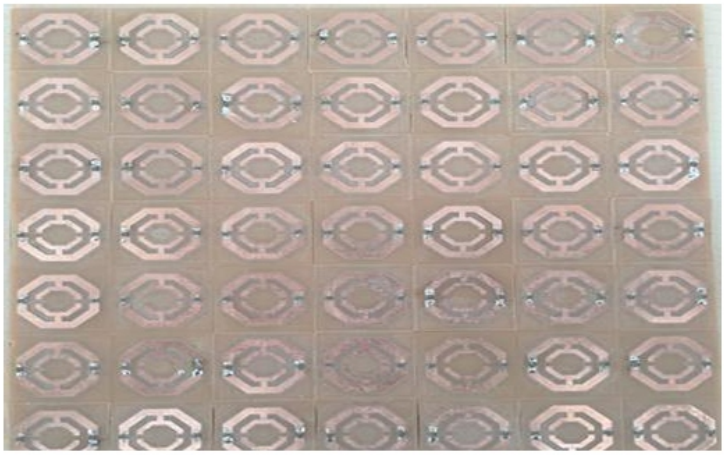

Fig. 15. Fabricated structure

In order to measure reflection coefficient, fabricated sample is placed in front of a horn antenna as shown in Fig. 16 and vector network analyser.

Fig. 16. Experimental setup for TEM mode wave

The free space measurements are obtained by using a horn antenna and a Vector Network Analyzer (VNA). The distance is set to 12.5 mm which is about 2.5 at 6 GHz. Since back side of the structure is covered by copper no transmission occurs on the proposed model. For this reason, measurement of the reflection (S11) is enough for the calculation of the absorptivity of the structure. In the experimental setup, only TEM mode measurements have been completed because of the laboratory capabilities. While measured and simulated reflection coefficient is presented in Fig. 17, absorption values) is given in Fig. 18.

The simulated and measured reflection coefficient resonance frequency have been observed at 6 Ghz. Simulation and experimental study results are complying with each other and similar results have been obtained. While simulated reflection coefficient in dB is -17 dB in simulation, the measured reflection

coefficient level is defined as -16 dB at 6 GHz as expected. In that frequency,) term is calculated as 0.98 which means that 98 % of the incident wave have been absorbed. The simulated and experimental study results show that the proposed structure can be used for energy harvesting application in WIMAX frequency band.

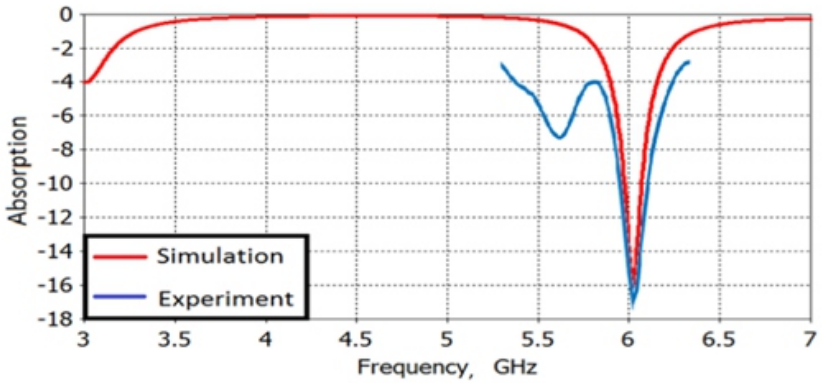

Fig. 17. Reflection (S11 in dB) of the simulation and experiment in TEM mode wave

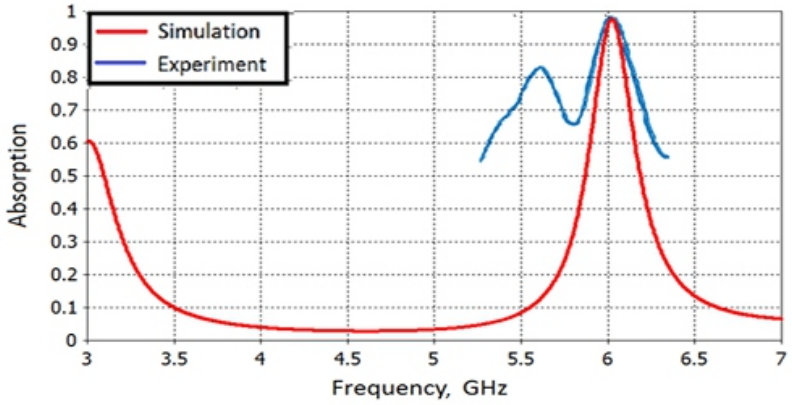

Fig. 18. Absorption of the simulation and the experiment in TEM mode wave

5. CONCLUSIONS

Nested octagonal shape metamaterial absorber model is numerically and experimentally designed and investigated in a wide perspective. Design details according to Resistor value, K, L, and gap parameter have been explained by simulation. Simulation results show that it is possible to tune the proposed structure with 1mm change in the dimension of L. Also simulation study results show that, maximum energy harvesting occurs when 325ohm resistor value usage in TE mode. Absorption mechanism is explained by giving electric field and surface current distributions. Energy harvesting efficiency of the proposed structure has been as 80 % between 5 and 6 GHz. These results show that the proposed structure can effectively be used as an energy harvester in these bands. Experimental study for

supporting the simulated study results have been given for reflection coefficient measurement in TEM mode. The fabricated sample is tested in the facility by using horn antenna and vector network analyser. Obtained results in reflection coefficient measurement show good agreement. According to simulation and experimental study results, the proposed structure can be used as energy harvester in the WIMAX communication band and this has a potential application in the area of absorption and energy harvesting applications. For the future works, this design can be developed for better performance in all application modes as well as sensor applications may be offered.

REFERENCES

1. Veselago, V.G. The Electrodynamics of Substances with Simultaneously Negative Values of and μ Soviet Physics Uspekhi 10 (4) 1968: pp. 509. https://doi.org/10.1070/PU1968v010n04ABEH003699

2. Shelby, R.A., Smith, D.R., Schultz, S. Experimental Verification of a Negative Index of Refraction Science 292 (5514) 2001: pp. 77 – 79. https://doi.org/10.1126/science.1058847

3. Schurig, D., Mock, J.J., Justice, B.J., Cummer, S.A., Pendry, J.B., Starr, A.F., Smith, D.R. Metamaterial Electromagnetic Cloak at Microwave Frequencies Science 314 (5801) 2006: pp. 977 – 980. https://doi.org/10.1126/science.1133628

4. Pendry, J.B., Schurig, D., Electromagnetic Fields 2006: pp. 1780 – 1782. Smith, D.R. Controlling Science https://doi.org/10.1126/science.1125907 312 (5781)

5. Fang, N., Lee, H., Sun, C., Zhang, X. Sub–diffractionLimited Optical Imaging with a Silver Superlens Science 308 (5721) 2005: pp. 534 – 537. https://doi.org/10.1126/science.1108759

6. He-Lin, G.L.Y.Y., Chao-Song, L.M.H.G., Yuan, T. A Mircostrip Antenna with Single Square Ring Structured Left-Handed Metamaterial Acta Physica Sinica 1 2012: pp. 021. https://doi.org/10.7498/aps.61.014102

7. Ziolkowski, R.W., Efficient Electrically Erentok, A. Metamaterial-Based Small Antennas IEEE Transactions on Antennas and Propagation 54 (7) 2006: pp. 2113 – 2130. https://doi.org/10.1109/TAP.2006.877179

8. Lim, S., Caloz, C., Itoh, T. Metamaterial-Based Electronically Controlled Transmission-Line Structure as a Novel Leaky-Wave Antenna with Tunable Radiation Angle and Beamwidth IEEE Transactions on Microwave Theory and Techniques 52 (12) 2004: pp. 2678 – 2690. https://doi.org/10.1109/TMTT.2004.839927

9. Melik, R., Unal, E., Perkgoz, N.K., Puttlitz, C., Demir, H. V.Metamaterial-Based Wireless Strain Sensors Physics Letters 95 (1) 2009: pp. 011106. https://doi.org/10.1063/1.3162336 10.

10. Sabah, C., Dincer, F., Karaaslan, M., Applied Unal, E., Akgol, O.,Demirel, E. Perfect Metamaterial Absorber with Polarization and Incident Angle Independencies Based On Ring and Cross-Wire

Resonators for Shielding and a Sensor Application Optics Communications 322 2014: pp. 137 – 142. https://doi.org/10.1016/j.optcom.2014.02.036

11. Sabah, C., Roskos, H.G. Broadside-Coupled Triangular Split-Ring-Resonators for Terahertz The European Physical Journal-Applied Physics 2013: pp. 30402 – 1:7. https://doi.org/10.1051/epjap/2013120053 Sensing 61 (3)

12. Dincer, F., Karaaslan, M., Colak, S., Tetik, E., Akgol, O., Altıntas, O., Sabah, C. Multi-Band Polarization Independent Cylindrical Metamaterial Absorber and Sensor Application Modern Physics Letters B 30 (08) 2016: pp. 1650095. https://doi.org/10.1142/S0217984916500950

13. Karaaslan, M., Bağmancı, M., Ünal, E., Akgol, O., Sabah, C. Microwave Energy Harvesting Based on Metamaterial Absorbers with Multi-Layered Square Split Rings for Wireless Communications Communications 392 2017: pp. 31 – 38. https://doi.org/10.1016/j.optcom.2017.01.043

14. Dincer, F., Karaaslan, M., Unal, E., Demirel, E., Sabah, C. Polarization and Angle Independent Perfect Metamaterial Absorber Based On Discontinuous Cross-Wire-Strips Journal of Electromagnetic Waves and Applications 28 (6) 2014: pp. 741 – 751. https://doi.org/10.1080/09205071.2014.888322

15. Landy, N.I., Sajuyigbe, S., Mock, J.J., Smith, D.R., Padilla, W.J. Perfect Metamaterial Absorber Review Letters 100 (20) 2008: pp. 207402. https://doi.org/10.1103/PhysRevLett.100.207402

16. Sen, G., Banerjee, A., Kumar, M., Islam, S.N., Das, S.A Dual Band Metamaterial Inspired Absorber for WLAN/WiMAX Applications Using a Novel I-Shaped Unit Cell Structure In Microwave Conference (APMC) 2016 AsiaPacific 2016: pp. 1 – 3. https://doi.org/10.1109/APMC.2016.7931413

17. Sabah, C. Multiband Metamaterials Based On Multiple Concentric Open-Ring Resonators Topology IEEE Journal of Selected Topics in Quantum Electronics 19(1) 2013: pp. 8500808 – 8500808. https://doi.org/10.1109/JSTQE.2012.2193875

18. Sabah, C. Novel, Dual Band, Single and Double Negative Metamaterials: Nonconcentric Delta Loop Resonators Progress In 2010: pp. 225 – 239. Electromagnetics https://doi.org/10.2528/PIERB10080302 Research

19. Urbani, F.Experimental Analysis of Novel Single-Sided Left-HandedMetamaterial IEEE Antennas and Wireless Propagation Letters 9 2010: pp. 720 – 723. https://doi.org/10.1109/LAWP.2010.2058837

20. Fernandes, H.C.C. Metamaterial Antennas and Finlines Using Full Wave Analysis In WSEAS International B25 Conference. Proceedings. Mathematics and Computers in Science and Engineering 2008: pp. 69 – 73.

21. Huang, L., Chen, H. Multi-Band and Polarization Insensitive Metamaterial Absorber Progress In Electromagnetics Research 113 2011: pp. 103 – 110. https://doi.org/10.1063/1.4878697

22. Bilotti, F., Nucci, L., Vegni, L. An SRR Based Microwave Absorber Microwave and Optical

Technology Letters 48 (11) 2006: pp. 2171 – 2175. https://doi.org/10.1002/mop.21891

23. Zhu, B., Wang, Z., Huang, C., Feng, Y., Zhao, J., Jiang, T. Polarization Insensitive Metamaterial Absorber with WideIncident Angle Progress In Electromagnetics Research 101 2010: pp. 231 – 239. https://doi.org/10.2528/PIER10011110

24. Dincer, F., Karaaslan, M., Unal, E., Delihacioglu, K., Sabah, C. Design of Polarization and Incident Angle Insensitive Dual-Band Metamaterial Absorber Based On Isotropic Resonators Progress In Electromagnetics Research 144 2014: pp. 123 – 132. https://doi.org/10.2528/PIER13111403

25. Cheng, Y., Yang, H. Design, Simulation, and Measurement of Metamaterial Absorber Journal of Applied Physics 108 (3) 2010: pp. 034906. https://doi.org/10.1063/1.3311964

26. Xie, Y., Fan, X., Chen, Y., Wilson, J.D., Simons, R.N., Xiao, J.Q. A Subwavelength Resolution Microwave/6.3 Ghz Camera Based on a Metamaterial Absorber Reports 7 2017: pp. 1 – 8. https://doi.org/doi:10.1038/srep40490

Effect of De-Ashing Strategies on Pore Structure and Electrochemical Performance of Activated Carbons for Supercapacitors

Weiwei KANG 1, 2, Guangxu HUANG 1, 3 , Qianhao GENG 1, Wentao HOU 1, Youheng YAO 1, Bing XU 1, Baolin XING 1, 3, Chuanxiang ZHANG 1, 3, 4

1 College of Chemistry and Chemical Engineering, Henan Polytechnic University, Jiaozuo 454003, China

2 School of Chemistry and Chemical Engineering, Southeast University, Nanjing 211189, China

3 Collaborative Innovation Center of Coal Work Safety, Henan Province

4 Henan Key Laboratory for Green and Efficient Mining & Comprehensive Utilization of Mineral Resources, Henan Polytechnic University

ABSTRACT

The ash was removed before or after carbonization of potassium humate to investigate the effect of ash removal methods on pore structure and electrochemical performance of activated carbons for supercapacitors. The activated carbons were prepared by direct carbonization of potassium humate at 700 ℃ for 1 hour under N2 atmosphere with different de-ashing strategies. It was found that ash removal before carbonization was an effective strategy to reduce the ash content of the corresponding activated carbon. When de-ashing treatment was adopted after carbonization, part of the ash in activated carbon was coated with carbon and could not be removed through acid soaking. Moreover, ash removal before carbonization could better contribute to creating the micropores and the ash removed after carbonization performed as templates to mainly generate mesopores. The activated carbon with ash removed before carbonization as electrodes delivered a specific capacitance of 164.84 F/g at a current density of 50 mA/g, and exhibited typical electric double layer capacitive performance as well as lower leakage current of 15.3 μA.

Keywords: ash removal, activated carbon, potassium humate, template, mesopores.

1. INTRODUCTION

Electric double layer capacitors (EDLCs), also known as supercapacitors, have been extensively investigated due to their excellent properties such as high power density, high coulombic efficiency, short charging time and long cycle life [1, 2]. EDLCs currently fill the gap between batteries and conventional capacitors [3 – 8], and have widespread applications in hybrid vehicles, memory backup – system [6, 7], elevator, locomotives [9], and so on. EDLCs store charges in the double layer formed at the electrolyteelectrode interface [3, 7, 10, 11], and their electrochemical performances strongly depend on the properties of the electrode materials, including specific surface area, pore size distribution, surface chemistry and electronic conductivity [12]. Activated carbon is considered as one of the most

promising electrode materials for EDLCs because of its high specific surface area, well-developed and adjustable porous structure, high conductivity, excellent chemical stability and low cost [4, 13].
Ash in activated carbon has negative impacts on the electrochemical properties of the corresponding EDLCs, including increase in leakage current and decrease in electrochemical cycling stability [12]. Fortunately, the mineral matter in precursors can function as templates for porosity formation of the resultant activated carbons [9]. Activated carbon prepared from rice husk, was basically mesoporous, which was obtained from leaching of the mineral component of silica, and exhibited a considerable specific capacitance of 120 F/g in EMIm.BF4 [14]. Qu [15] prepared corncob residues based porous carbon with high capacitance of 314 F/g and superb cycling stability in 6 M KOH electrolyte, and found that the process of ash removal was efficient for pore-forming, especially so for welldeveloped micropores. However, to the best of my knowledge, there are few studies available regarding the effects of the de-ashing strategies on the surface area and pore size distribution of the resulting activated carbons, which play a crucial role in determining their electrochemical performances.

Activated carbons for supercapacitors have been prepared from different precursors, including coal [3], coal tar pitch [16] and biomass [17]. Humic acid (HA), a kind of biomasses, consisting of a skeleton of aromatic units crosslinked by oxygen-containing functional groups [18, 19], has been becoming a promising precursor for activated carbon preparation. Oxygen-rich and hierarchical porous carbons were prepared from humic acid through KOH or ZnCl2 activation method, delivering high specific capacitance, high rate capabilities and excellent cycling stabilities [19 – 21]. Potassium humate, a neutralized product of KOH and HA with a KOH/HA mass ratio of about 0.12, can be used as precursor to synthesize highly porous carbons by single-step carbonization, which exhibited a high specific capacitance of 232 F/g (26.1 F/cm2) at a constant charge/discharge current of 0.5 A/g [22]. Obviously, the ash content of as-prepared porous carbons greatly depends on that of potassium humate due to the relatively weak activation with small amount of potassium. In other words, potassium humate is an appropriate precursor for preparing activated carbons as EDLCs electrodes and, more importantly, for studying the effects of de-ashing strategies on their pore structure simultaneously.

In this paper, the commercial potassium humate with high ash content is adopted as precursor to prepare activated carbons by direct carbonization with ash removed before or after carbonization, respectively. The effects of ash removal strategies on the specific surface area and pore size distribution of as-prepared activated carbons are studied, and their electrochemical properties are also investigated in detail.

2. EXPERIMENTAL

2.1. Preparation of activated carbons

The commercial potassium humate with ash content of 20 % was purchased from Shuanglong Co., Ltd (Xinjiang, China) and its ultimate analysis is shown in Table 1. The activated carbons were prepared by direct carbonization of potassium humate at 700 ° for 1 hour with a heating rate of 5 °C/min under N2 flow. The ash was removed before or after carbonization of commercial potassium humate through hydrochloric acid and hydrofluoric acid soaking with a volume ratio of 1:1. The carbonized materials were washed with diluted hydrochloric acid and deionized water, and dried at 120 ° for 2 hours. The obtained activated carbons with ash removed before or after carbonization were referred as AC1 and AC3, respectively. Meanwhile, activated carbon prepared without ash removed was nominated as Ac2.

Table 1. Ultimate analysis of potassium humate

C_{daf}, %	H_{daf}, %	$(O + S)^*_{daf}$, %	N_{daf}, %
44.98	3.26	50.85	0.91
Notes: ad – air dried basis; d – dry basis; daf – dry ash free basis; * – difference method.			

2.2. Characterization

The elemental composition of porous carbons was analyzed by an elemental analyzer (Vario Macro Cube, Germany). A silica crucible and a muffle furnace were used to estimate ash content. X-ray diffraction (XRD) patterns were collected on a Rigaku Smart-Lab X-ray diffractometer at a scan rate of 10 °C/min. N2 adsorption/desorption isotherms were measured using a Quantachrome AutosorbiQ-MP analyzer at 77 K. The specific surface area (SBET) was calculated from the isotherms using Brunauer-EmmettTeller method. The total pore volume (Vt) was estimated from the single point adsorption (P/P0 = 0.99) and pore size distributions (PSD) were derived from density functional theory (DFT). The micropore volume (Vmic) was determined by the t-plot method and the mesopore volume (Vmes) was calculated by the difference of total pore volume and micropore volume. Prior to test, the samples were degassed at 200 °C for 10 hours to remove the water vapor and other foreign gas matters. The morphology of the samples was observed by scanning electron microscope (SEM, JSM 6390LV, JEOL). X-ray photoelectron spectroscopy (XPS, Thermo ESCALAB 250Xi) was used to investigate the surface chemical composition.

2.3. Electrodes preparation and electrochemical measurements

A two-electrode cell was used for electrochemical tests with a 3 M KOH solution as the electrolyte. The electrodes were fabricated by mixing 85 wt.% activated carbon powders with 10wt% of acetylene black

and 5wt% of polytetrafluorene ethylene (PTFE) binder. The galvanostatic charge-discharge (GCD), cyclic voltammetry (CV) and Leakage current (LC) were performed on an Arbin SCTS Instrument (CSCT, Arbin, USA). The gravimetric capacitances (F/g) were calculated from the discharge curves according to:

$$C_g=2(I\,\Delta t)/(m\,\Delta V), \qquad (1)$$

where I, t, m and V are the discharge current, A; discharge time, s; the mass, g of the active materials in the single electrode and the discharge voltage, respectively.

3. RESULTS AND DISCUSSION

3.1. Characterization of pore structure

The ash contents of the three activated carbons are listed in Table 2. The commercial potassium humate precursor has high ash content of 20 %, resulting in relatively high ash content (11.6 %) of the corresponding activated carbon (AC2) without ash removal in the preparation process.

Table 2. Ash contents of the activated carbons

Samples	AC1	AC2	AC3
Ash, %	6.3	11.6	9.4

The three carbons have an order of AC1 < AC3 < Ac2 in terms of ash content. The result indicates that ash removal before rather than after carbonization is an effective strategy to reduce the ash content of the corresponding activated carbons, and also suggests that part of the ash in AC2 is coated with carbon and cannot be removed through acid soaking.

As shown in Fig. 1, activated carbons all exhibit two broad peaks at around 2 = 22° and 43°, which are attributed to the reflection in the (002) plane and (100) plane of aromatic layers respectively, indicating a porous structure with a relatively low degree of graphitization [23].

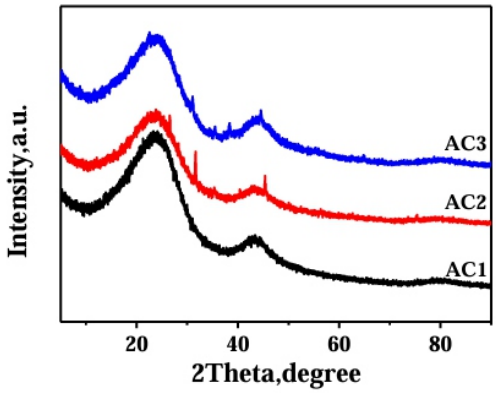

Fig. 1. XRD patterns of activated carbons

For AC2 and AC3, there are some sharp peaks, which is assigned to the mineral matters.

Fig. 2 a shows the N2 adsorption/desorption isotherms of activated carbons. The isotherms of AC1 and AC3 exhibit characteristics of type IV curve, showing a sharp increase in adsorptive volumes at low relative pressures while a relatively smooth increase at high relative pressure, and exhibiting pronounced hysteresis loops. The results above demonstrate the presence of certain amount of micropores and mesopores in AC1 and AC3. The N2 adsorption/desorption isotherm of AC2 exhibits combined characteristics of type I/IV curve. The obvious hysteresis loop indicates the existence of a relatively large percentage of mesopores, and the almost vertical tail at a relative pressure near to 0.95 denotes the presence of macroporosity [12, 13, 20].

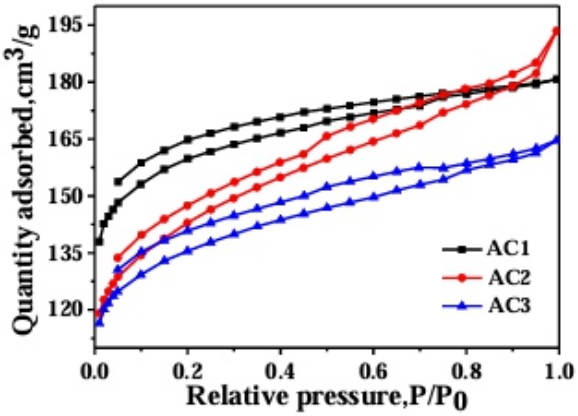

a

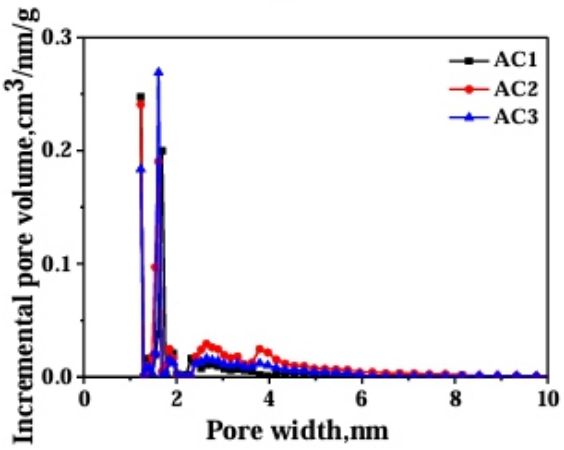

b

Fig. 2. a – N2 adsorption-desorption isotherms of activated carbons; b – pore size distribution of activated carbons The PSD curves are shown in Fig. 2 b and demonstrate activated carbons possess hierarchical pore structure with micropores less than 1.8 nm and mesopores in the range of 2.3 to 6 nm. It is well known that the micropores can accommodate electrolyte ions to achieve high capacitance, mesopores act as channels to facilitate ion transportation within the carbon framework, and macropores serve as ionbuffering reservoirs to reduce diffusion distance for electrolyte ions diffusing into the interior surface [9, 10]. Therefore, the as-prepared activated carbons used as electrodematerials for the

supercapacitors may exhibit excellent performance [6 – 8, 23].

The pore structure parameters of the activated carbons are summarized in Table 3. AC1 exhibits higher specific surface area and micropore volume while smaller mesopore volume and mesoporosity than AC2, indicating that the mineral matter in precursor facilitates the mesopores formation, however, suppresses the micropores formation that is tightly associated with specific surface area.

Compared to AC2, AC3 shows approximately equal value of micropore volume, slight increase of specific surface area but significant increase in mesopore volume (nearly doubled), which suggest that the ash removal of activated carbon mainly influence the mesopore rather than micropore formation. In summary, among the three activated carbons, AC1 possesses the largest specific surface area of 492 m2/g and micropore volume of 0.2279 cm3/g, AC3 possesses the largest total pore volume, mesopore volume and mesoporosity, and AC2 possesses the smallest specific surface area, total pore volume and micropore volume.

Potassium humate is a neutralized product of KOH and HA with a KOH/HA mass ratio of about 0.12. During carbonization of potassium humate, the small amount of potassium prefers to react with mineral matter to form mesopores, thus, the reaction between potassium and organic matter to create micropores is weakened. That is, the ash in potassium humate may suppress the formation of micropores and benefit the formation of mesopores. Obviously, the degree of reaction to make mesopores in commercial potassium humate is higher than that in pure potassium humate, which is contrary in terms of the reaction of forming micropores. AC3 exhibits more remarkable increment of mesopore volume than AC2, which is due to the micropore wall collapsing and template effect based on ash removal from Ac2.

Table 3. Specific surface area and pore structure parameters of activated carbons

Samples	S_{BET}, m^2/g	V_t, cm^3/g	V_{mic}, cm^3/g	V_{mes}, cm^3/g	$(V_{mes})/V_t$, %
AC1	492	0.2498	0.2279	0.0217	8.7
AC2	421	0.2270	0.1916	0.0353	15.6
AC3	451	0.2599	0.1928	0.0670	25.8

The surface morphologies of the samples are presented in Fig. 3. AC1 displays blocky structure with plenty of pores on its rough surface, which originates from the properties of potassium humate, i.e., certain order degree and relatively low ash content. AC2 exhibits three-dimensionally loose and amorphous structure with interconnected pores. Ac3 shows the thick lamellar structure derived from aromatic units and these individual sheets associate with each other to form a continuous network.

The surface chemical compositions of activated carbons were analyzed by XPS measurements. As

shown in Fig. 4, activated carbons all possess two main peaks located at the binding energy of about 285 and 533 eV, which correspond to the C1s and O1s, respectively. The C1s spectrum can be approximately fitted into four main peaks located at the binding energy of 284.5 eV, 285.2 eV, 286 eV and 289 eV, which is related to the sp2 hybridized carbon (Cp1), sp3 hybridized carbon (Cp2), C-O (Cp3) as well as C = O (Cp4) functional groups, respectively. The presence of oxygen containing functional groups can improve the wettability of activated carbons, and facilitate the penetration of electrolytes to pores.

3.2. Electrochemical properties

The carbon and oxygen contents of activated carbons are all in the range of 82.2 – 83.8 wt.%, 12.2 – 13.8 wt.%,

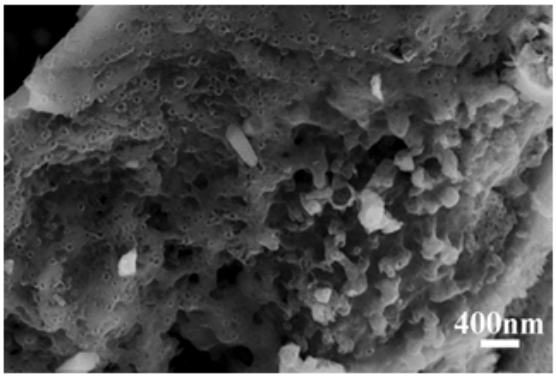

a

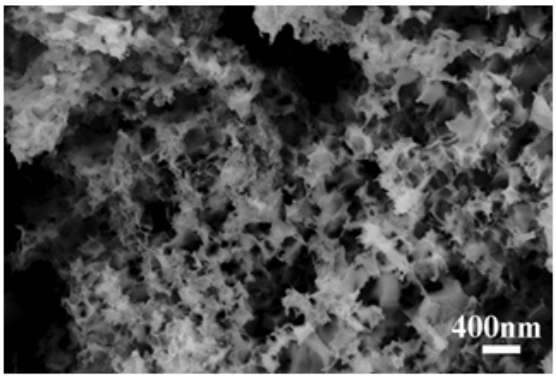

b

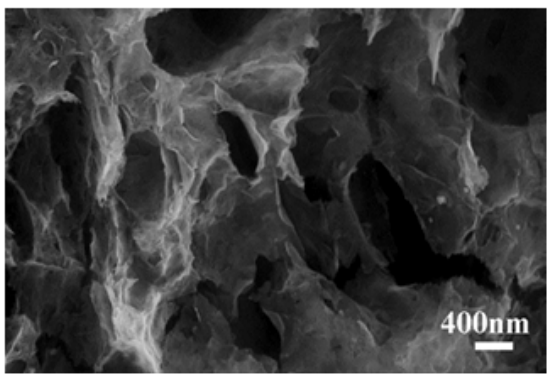

c

Fig. 3. SEM images of activated carbons: a – AC1; b – Ac2; c – Ac3

Thus, the electrochemical properties of the samples may mainly depend on their pore structures and ash contents. The GCD curves of the activated carbons as electrodes presented in Fig. 5 a exhibit typical triangular shapes without obvious voltage drop at the beginning of discharge, indicating the electrodes have the typical capacitive behaviors [21]. Moreover, the specific capacitances calculated from Eq. 1 are 164 F/g for AC1, 110 F/g for AC2 and 127 F/g for AC3, respectively. It is known that micropores can provide electrode materials with a high accessible surface area for double layer capacitance. The three carbons have an order of AC1 > AC3 > AC2 in terms of the specific capacitance, which agrees well with the order of the specific surface areas.

The CV curves of activated carbons at the scan rate of 1 mV/s (Fig. 5 b) exhibit a quasi-rectangular shape without visible distortion, indicating the double layer capacitive behavior and excellent electrochemical reversibility, which is consistent with the results of GCD curves.

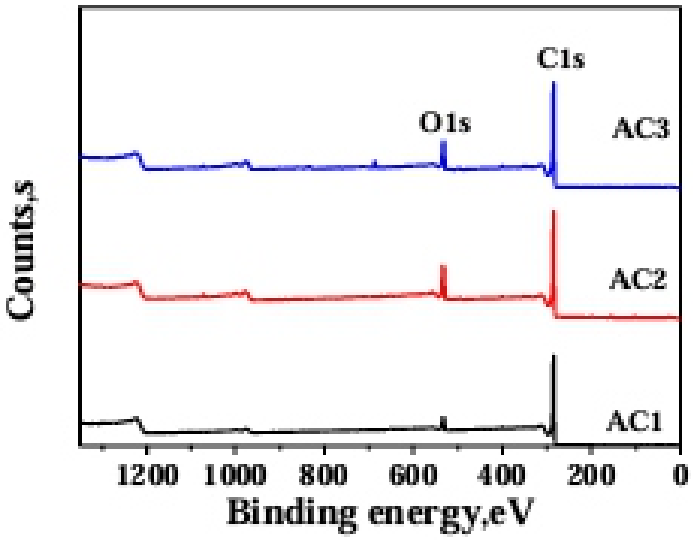

a

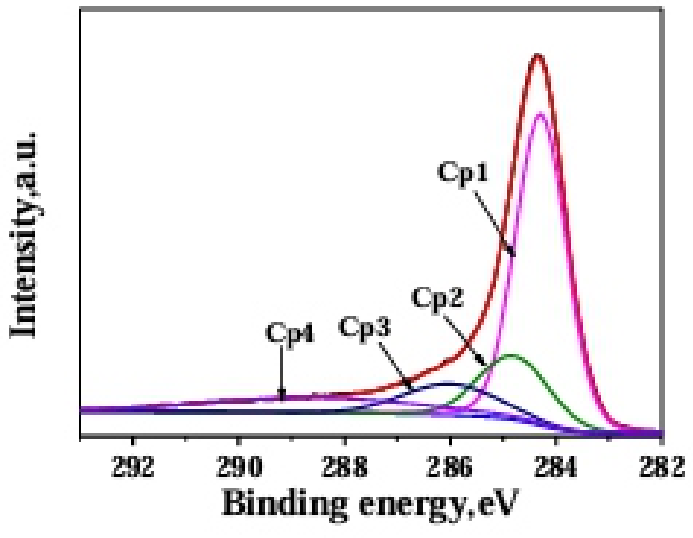

b

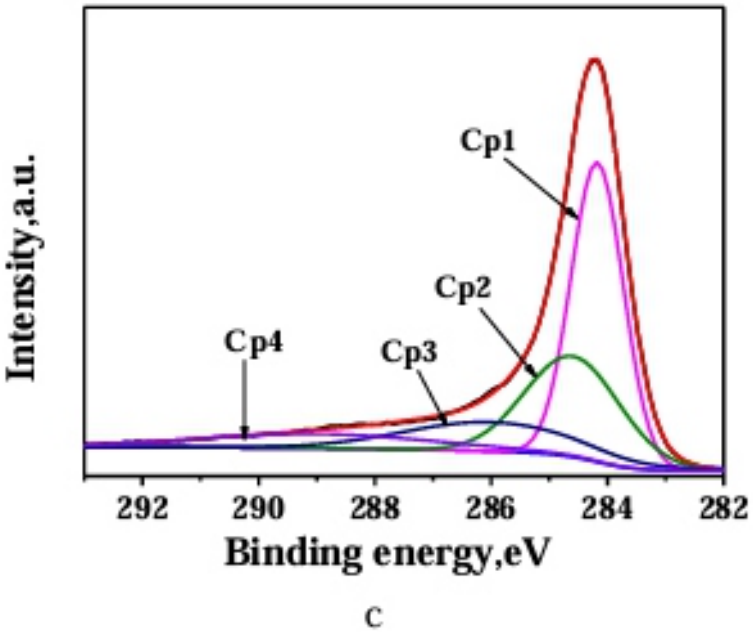

c

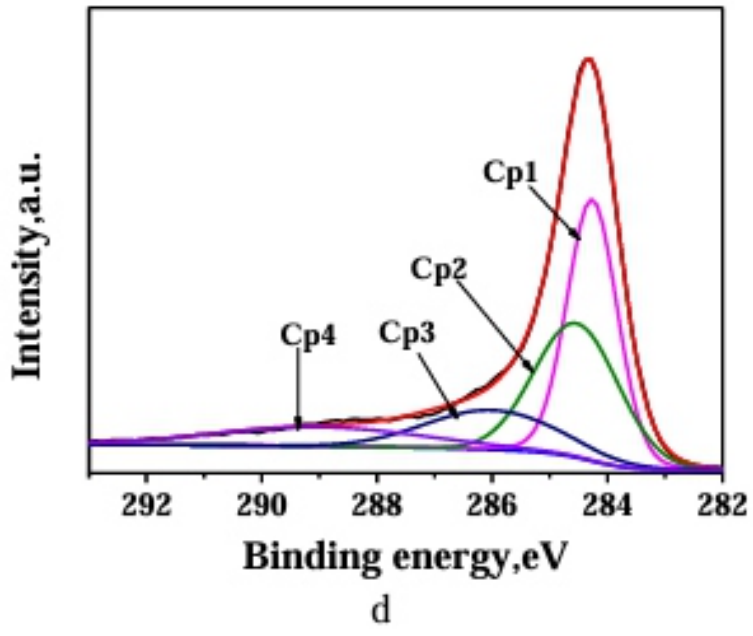

d

Fig. 4. a – full-range XPS spectrum of activated carbons; b – C1s XPS spectrum of AC1; c – C1s XPS spectrum of AC2; d. C1s XPS spectrum of Ac3

Leakage current is a main parameter on practical applications of the EDLCs. As shown in Fig. 5 c, the leakage currents of AC1 and AC3 drop significantly from 0.906 mA to 0.104 mA at the beginning 17 min, while that of AC2 is from 0.886 mA to 0.106 mA after 34 min. Then they all gradually become smaller and more stable (finally to only 15.3 μA for AC1, 25.0 μA for AC2 and 17.3 μA for AC3 after 5.4 hours, respectively). The leakage current behavior is related to the ash content, the values of leakage current and ash contents follow the same sequence of AC1 < AC3 < AC2. The smaller values of leakage

current mean less shuttle reactions caused by the ashes in the activated carbons [21]. The less ash content, the smaller leakage current, which is in according to the results in the literature [12].

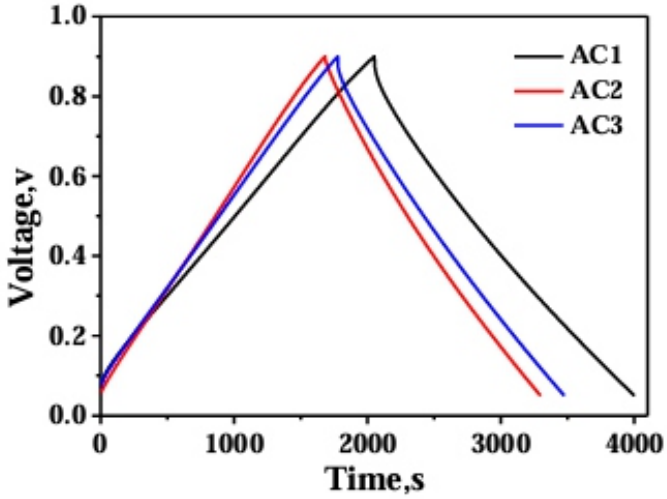

a

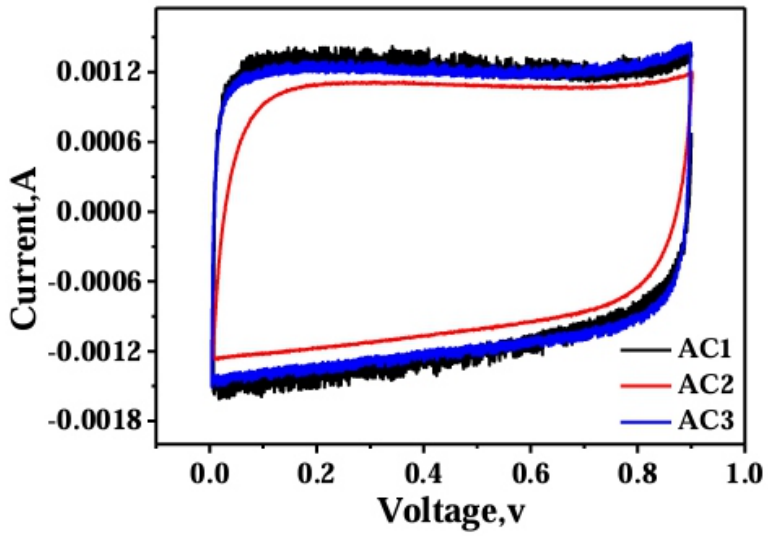

b

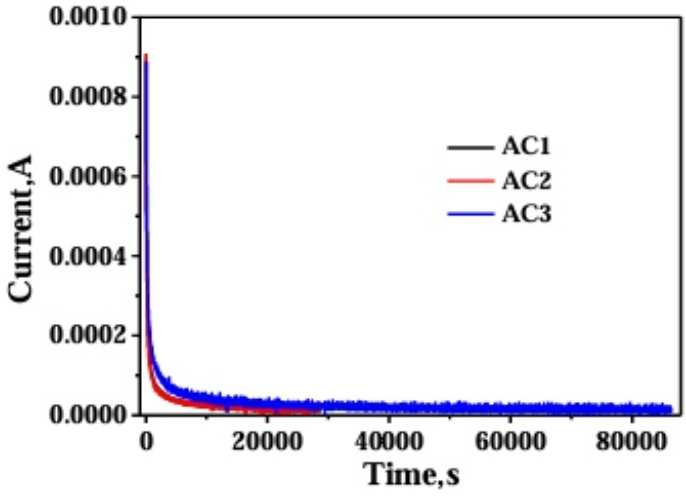

c

Fig. 5. a – GCD curves of activated carbons at 50 mA/g; b – CV curves of activated carbons at 1 mV/s; c – leakage current curves of activated carbons

4. Conclusions

The ash removal methods have an important effect on ash content, pore structure and electrochemical performance of corresponding activated carbons for electric double layer capacitors. The process of ash removal before carbonization can better contribute to creating the micropores and ash removed after carbonization performs as templates to mainly generate mesopores. The activated carbons possess large specific surface area of 492 m2/g, total pore volume of 0.2599 cm3/g, and micropore volume of 0.2279 cm3/g, respectively. The activated carbon (AC1) with ash removed before carbonization as electrodes delivers a specific capacitance of 164.84 F/g at a current density of 50 mA/g, v and exhibits typical electric double layer capacitive performance as well as lower leakage current of 15.3 μA.

Acknowledgements

This work is financially supported by the National Natural Science Foundation of China (U1361119, 51404098, 51174077), the Foundation of Henan Polytechnic University for Ph. D (B2014-008), Natural Science Foundation of Henan province (162300410115), Key Scientific Research Project of Colleges and Universities in Henan Province (18A440002) and the research fund of Henan Key Laboratory for Green and Efficient Mining & Comprehensive Utilization of Mineral Resources (Henan Polytechnic University).

REFERENCES

1. Meryl, S.P.Y.Z., Stoller, D. Graphene-Based Ultracapacitors Nano Letters 8 2008: pp. 3498 – 3502. https://doi.org/10.1021/nl802558y

2. Zhang, S., Pan, N. Supercapacitors Performance Evaluation Advanced Energy Materials 5 2015: pp. 1401401. https://doi.org/10.1002/aenm.201401401

3. Xing, B., Guo, H., Chen, L., Chen, Z., Zhang, C., Huang, G., Xie, W., Yu, J. Lignite-derived High Surface Area Mesoporous Activated Carbons for Electrochemical Capacitors Fuel Processing Technology 138 2015: pp. 734 – 742. https://doi.org/10.1016/j.fuproc.2015.07.017

4. Long, C., Jiang, L., Wu, X., Jiang, Y., Yang, D., Wang, C., Wei, T., Fan, Z. Facile Synthesis of Functionalized Porous Carbon with Three-Dimensional Interconnected Pore Structure for High Volumetric Performance Supercapacitors Carbon 93 2015: pp. 412 – 420. https://doi.org/10.1016/j.carbon.2015.05.040

5. Zhang, Y., Zhang, C., Huang, G., Xing, B., Duan, Y. Synthesis and Capacitive Properties of Manganese Oxide Nanoparticles Dispersed on Hierarchical Porous Carbons Electrochimica Acta

166 2015: pp. 107 – 116. https://doi.org/10.1016/j.electacta.2015.03.073

6. Chen, X.Y., Song, H., Zhang, Z.J., He, Y.Y. A rational Template Carbonization Method for Producing Highly Porous Carbon for Supercapacitor Application Electrochimica Acta 117 2014: pp. 55 – 61. https://doi.org/10.1016/j.electacta.2013.11.098

7. Cheng, Q., Tang, J., Ma, J., Zhang, H., Shin, N., Qin, L. Graphene and carbon nanotube composite electrodes for supercapacitors with ultra-high energy density PHYS CHEM CHEM PHYS 39 2011: pp. 17615 – 17624. https://doi.org/10.1039/c1cp21910c

8. Inal, I.I.G., Holmes, S.M., Banford, A. Aktas, Z. The Performance of Supercapacitor Electrodes Developed from Chemically Activated Carbon Produced from Waste Tea Applied Surface Science 357 2015: pp. 696 – 703. https://doi.org/10.1016/j.apsusc.2015.09.067

9. Jin, H., Wang, X., Gu, Z., Polin, J. Carbon materials from High Ash Biochar for Supercapacitor and Improvement of Capacitance with HNO3 Surface Oxidation Journal of Power Sources 236 2013: pp. 285 – 292. https://doi.org/10.1016/j.jpowsour.2013.02.088

10. Wang, G., Zhang, L., Zhang, J. A Review of Electrode Materials for Electrochemical Supercapacitors Chemical Society Reviews 41 2012: pp. 797 – 828. https://doi.org/10.1039/C1CS15060J

11. Braghiroli, F.L., Fierro, V., Szczurek, A. Stein, N., Parmentier, J., Celzard, A. Hydrothermally treated Aminated Tannin as Precursor of N-Doped Carbon Gels for Supercapacitors Carbon 90 2015: pp. 63 – 74. https://doi.org/10.1016/j.carbon.2015.03.038

12. Shao-yun, Z., Xin-hai, L., Zhi-xing, W., Hua-jun, G., Wen-Jie, P. Effect of Activated Carbon and Electrolyte on Properties of Supercapacitor Transactions of Nonferrous Metals Society of China 17 2007: pp. 1328 – 1333. https://doi.org/10.1016/S1003-6326(07)60271-4

13. Wasiński, K., Walkowiak, M., Lota, G. Humic acids as Pseudocapacitive Electrolyte Additive for Electrochemical Double Layer Capacitors Journal of Power Sources 255 2014: pp. 230 – 234. https://doi.org/10.1016/j.jpowsour.2013.12.140

14. Kumagai, S., Tashima, D. Electrochemical performance of Activated Carbons Prepared from Rice Husk in Different Types of Non-Aqueous Electrolytes Biomass & Bioenergy 83 2015: pp. 216 – 223. https://doi.org/10.1016/j.biombioe.2015.09.021

15. Qu, W., Xu, Y., Lu, A., Zhang, X., Li, W. Converting Biowaste Corncob Residue into High Value Added Porous Carbon for Supercapacitor Electrodes Bioresource Technology 189 2015: pp. 285 – 291. https://doi.org/10.1016/j.biortech.2015.04.005

16. He, X., Li, R. Qiu, J., Xie, K., Ling, P., Yu, M., Zhang, X., Zheng, M. Synthesis of Mesoporous Carbons for Supercapacitors from Coal Tar Pitch by Coupling Microwave-Assisted KOH Activation with a MgO Template Carbon 50 2012: pp. 4911 – 4921. https://doi.org/10.1016/j.carbon.2012.06.020

17. Chen, H., Liu, D., Shen, Z., Bao, B., Zhao, S., Wu, L. Functional Biomass Carbons with Hierarchical Porous Structure for Supercapacitor Electrode Materials Electrochimica Acta 180 2015: pp. 241 – 251. https://doi.org/10.1016/j.electacta.2015.08.133

18. Wasiński, K., Walkowiak, M., Lota, G. Humic Acids as Pseudocapacitive Electrolyte Additive for Electrochemical Double Layer Capacitors Journal of Power Sources 255 2014: pp. 230 – 234. https://doi.org/10.1016/j.jpowsour.2013.12.140

19. Xing, B., Guo, H., Chen, L., Zhang, C., Huang, G., Yi, G., Ma, M. Preparation of Oxygen-enriched Activated Carbons from Coal-based Humic Acids by Zinc Chloride Activation Current Nanoscience 11 2015: pp. 439 – 446. https://doi.org/10.2174/1573413711666150202234221

20. Huang, G., Kang, W., Xing, B., Chen, L., Zhang, C. Oxygen-rich and Hierarchical Porous Carbons Prepared from Coal Based Humic Acid for Supercapacitor Electrodes Fuel Processing Technology 142 2016: pp. 1 – 5. https://doi.org/10.1016/j.fuproc.2015.09.025

21. Zhang, Y., Zhang, C., Huang, G., Xing, B., Duan, Y. Tailoring the Textural Properties of Hierarchical Porous Carbons for Supercapacitors Materials Letter 159 2015: pp. 377 – 380. https://doi.org/10.1016/j.matlet.2015.07.020

22. Luo, H., Yang, Y., Chen, Y., Zhang, J., Zhao, X. Structure and Electrochemical Performance of Highly Porous Carbons by Single-Step Potassium Humate Carbonization for Application in Supercapacitors Journal of Applied Electrochemistry 46 2016: pp. 113 – 121. https://doi.org/10.1007/s10800-015-0894-0

23. Xing, B., Huang, G., Chen, Z., Chen, L., Yi, G., Zhang, C. Facile preparation of Hierarchical Porous Carbons for Supercapacitors by Direct Carbonization of Potassium Humate Journal of Solid State Electrochemistry 2017: pp. 263 – 271. https://doi.org/10.1007/s10008-016-3360-y

Characteristics and Sinterability of Ceria Stabilized Zirconia Nanoparticles Prepared by Chemical Methods

Jānis GRABIS , Dzidra JANKOVIČA, Ints ŠTEINS, Māra LUBĀNE, Inta SĪPOLA
Institute of Inorganic Chemistry, Faculty of Material Sciences and Applied Chemistry, Rīga Technical University, Kalku 1, Riga, LV-1658, Latvia

A B S T R A C T

Microwave assisted and molten salts synthesis were extended for preparation of ceria (10 mol%; 15 mol%) stabilized zirconia and their parameters and sinterability were compared with that of particles prepared by the sol-gel combustion method. As-prepared powders by using microwave assisted and sol-gel combustion synthesis contained single tetragonal ZrO2 phase but powders prepared by molten salts combustion method contained two ceria-stabilized tetragonal phases with different content of ceria. The crystallite size of the as-prepared zirconia phases was in the range of 3.2 – 9.4 nm and the average particles size is in the range of 7.6 – 24.6 nm depending on the synthesis method. Additional calcination of the powders up to 1000 °C led to increase of crystallite size in the range of 19 – 25 nm and decrease of specific surface area in the range of 18 – 21 m2/g and partial formation of monoclinic phase of ZrO2. Bulk materials with fine-grained microstructure (0.8 – 1.6 μm) and density in the range of 95.2 – 97.2 % were obtained by spark plasma sintering at 1280 – 1310 °C during 3 min. Nanoparticles prepared by microwave assisted synthesis showed better sinterability and higher density.

Keywords: zirconia, ceria, synthesis of nanoparticles, spark plasma sintering.

1. INTRODUCTION

Ceria stabilized zirconia polycrystalline ceramics have been investigated extensively due to their better stability relate to yttria-stabilized zirconia in the moist environment [1] and the thermal expansion coefficient matching that of the iron-alloys [2]. However, mechanical characteristics of ceria-stabilized zirconia depend on its density, grain-size and presence of the transformable tetragonal phase [2, 3] which depends on the used preparation route of powders and their sintering method. Nanosized powders with a high specific surface area with definite phase composition and fast their sintering methods are required for manufacturing of dense fine-grained zirconia based ceramic. Several chemical methods such as spray-drying [2], hydrothermal [4], sol-gel [5, 6], sol-gel-combustion [6, 7, 8], coprecipitation [8] have been developed for preparation of nanosized stabilized zirconia nanopowders.

Each preparation method of ceria stabilized zirconia nanoparticles has its characteristic advantages and disadvantages that relate mainly to complexity of the process, expensive precursors, production rate and

cost as well as to size distribution of the particles and presence of agglomerates. Present trends in technology are directed to development of effective and environmentally friendly preparation methods of nanoparticles. From this point of view, fast microwave assisted and solvent free molten salt synthesis [9], which has been successful applied for producing several nanoparticles, is a promising preparation method of ceria stabilized zirconia.

The aim of the present work was extension of microwave assisted and molten salt preparation methods for the synthesis of ceria stabilized zirconia nanoparticles and comparison of the characteristics and sinterability of the obtained powders with that of the particles produced by the sol-gel combustion method.

2. EXPERIMENTAL

Synthesis was performed by using the following analytical reagent grade chemicals: ZrOCl2.8H2O, Ce(NO3)2.6H2O, urea CH4N2O, glycine C2H5NO3, NaClNaNO3.

For molten salts (MS) synthesis, the zirconium and cerium salts were mixed and grounded with a definite amount of NaCl and NaNO3. The mixture of the zirconium and cerium salts contained 10 or 15 mol% of CeO2. The molar ratio of Zr and Ce to Na salts was in the range of 0.12 – 0.25. A crucible with precursors was put into the furnace and heated at 400 – 800 °C high temperature during 2 h. The melting temperature of Na salts was changed by varying the ratio of sodium salts. The obtained ZrO2 nanoparticles were extracted from the cooled products by dissolving sodium salts in distilled water and washing with ethanol, followed by filtration. The microwave assisted synthesis (MW) of ZrO2 was performed by using the Masterwave BTR (Anton Paar) reactor. The zirconium and cerium salts were dissolved in distilled water (0.25 mol/L) and stirred for 30 min. Then glycine water solution was added (molar concentration of glycine/metal atoms was 4:1). The prepared mixture was heated in the microwave reactor at 160 – 180 °C during 20 min with continuous stirring. The obtained particles were extracted by filtration and washed with distilled water and ethanol.

For sol-gel combustion (SG) synthesis [6] ZrOCl2.8H2O was dissolved in distilled water and HNO3 was added to replace Cl- ions. Mixture was stirred for 30 min at 80 °C and then a definite amount of Ce(NO3)2.6H2O water solution was added. Concentration of the solution was 0.25 mol/L. Additionally solution of glycine and HNO3 was added in order to reach the molar ratio metals/glycine = 0.5 and glycine/NO3- = 0.7. The prepared solution was calcinated up to 120 – 130 °C on a hot plate until a dark viscous gel was formed and finally burned. The reaction product was calcinated at 400 °C for 2 h.

All prepared samples of ceria-stabilized zirconia were calcinated up to 1000 °C temperature in order to examine their thermal stability and phase transition. The nanocrystalline powders were pressed into graphite dies with diameter of 20 mm and densified in vacuum at 1200 – 1500 °C and pressure of 30 MPa

using the spark plasma sintering (SPS) technique (SPS-825.CE). The phase composition of the powders was determined by the X-ray diffraction (XRD) analysis (Advanced D8, Bruker AXS). Crystallite size D was calculated by using X-ray diffraction software Eva12 based on the Scherrer formula. The specific surface area (SSA) of the powders was determined by the argon absorption-desorption method. The average particle size d was calculated from SSA; agglomeration degree of the particles was evaluated from ratio d/D [6]. Density of the bulk materials was determined by using the Archimede's method. Microstructure of the materials was examined by scanning electron microscopy (SEM) LYRA3. Vickers hardness was determined by the identation technique.

3. RESULTS AND DISCUSSION

Typical temperature of the microwave, molten salts and sol-gel combustion synthesis and characteristics of the prepared ceria-stabilized zirconia are shown in Table 1.

Table 1. Characteristics of as-prepared ZrO2-10 mol% CeO2 nanoparticles

Synthesis method	Synthesis temperature, °C	SSA, m^2/g	Crystallite size *D*, nm	Average particle size *d*, nm	Ratio *d/D*
MW	170	120.2 ± 0.6	3.2 ± 0.4	7.8 ± 0.5	2.4
MW	180	92.1 ± 0.5	3.6 ± 0.4	10.2 ± 0.5	2.8
MS	400	123.1 ± 0.6	5.3 ± 0.4	7.6 ± 0.5	1.4
MS	600	109.0 ± 0.5	5.8 ± 0.4	8.5 ± 0.5	1.5
SG	500	48.2 ± 0.3	8.2 ± 0.3	19.5 ± 0.4	2.1
SG	600	39.2 ± 0.3	9.4 ± 0.3	24.6 ± 0.4	2.6

The nanoparticles prepared by MW and MS synthesis had higher SSA and lower crystallite size with respect to the powders obtained by the SG process. The SSA for all processes depended on the temperature. However, nanoparticles prepared by the molten salt synthesis method had highest SSA despite the higher temperature of synthesis as that of the microwave assisted process. It indicated that liquid salts prevented growth of the ceria-zirconia nanoparticles.

The dependence of SSA of the nanoparticles prepared The nanoparticles prepared by MW and MS synthesis had higher SSA and lower crystallite size with respect to the powders obtained by the SG process. The SSA for all processes depended on the temperature. However, nanoparticles prepared by the molten salt synthesis method had highest SSA despite the higher temperature of synthesis as that of the microwave assisted process. It indicated that liquid salts prevented growth of the ceria-zirconia nanoparticles. The dependence of SSA of the nanoparticles prepared by MS synthesis on ratio metals/salts (Fig. 1) confirmed influence of salts. Decrease of oxide content in mixture remarkably

increased the SSA of nanoparticles prepared by the MS method.

The crystallite size of as-prepared by the MW and MS methods nanoparticles were in the range of 3.2 – 5.8 nm but the crystallite size of nanoparticles prepared by SG method was in the range of 8.2 – 9.4 nm. These data indicated that the crystallite size of the particles depended on synthesis method, synthesis temperature and time. Low temperature and short duration of the MW process (20 min) promoted formation of smaller crystallites.

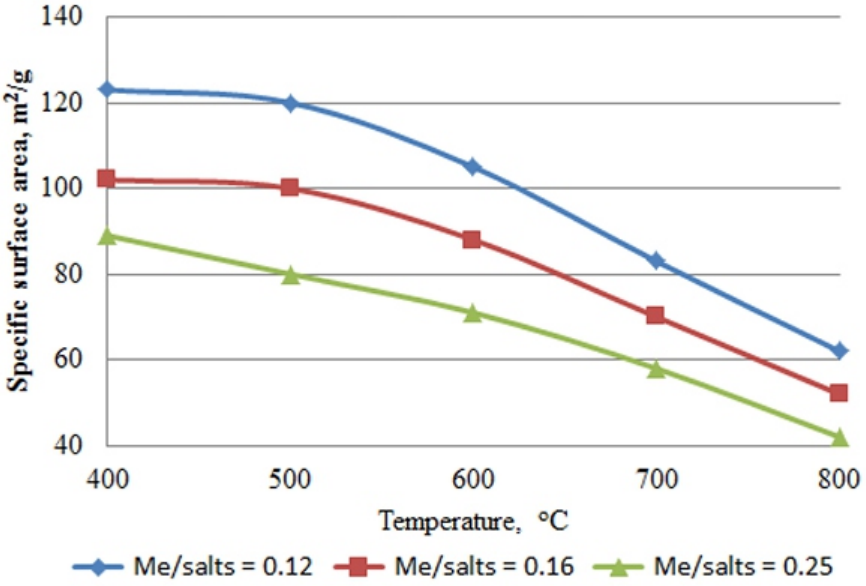

Fig. 1. Dependence of the SSA of the samples produced by MS synthesis on the calcination temperature for different ratio metal/salts (Me/salts)

Values of the average particle size d calculated from SSA exceeded the determined crystallite size D 1.4 – 2.6 times. The ratio d/D that indicated degree of agglomeration [6] was smaller for nanoparticles prepared by the MS method because liquid salts as well as repeated washing of the products with water and ethanol prevented agglomeration and decreased its degree. XRD patterns of as-prepared nanoparticles showed broad diffraction patterns of the ceria-stabilized tetragonal phase of zirconia (Fig. 2).

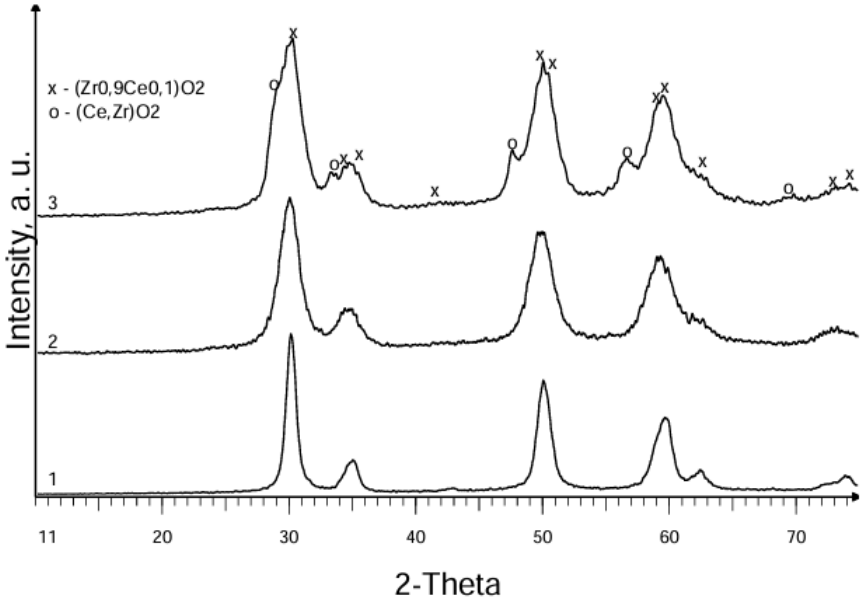

Fig. 2. XRD patterns of the as-prepared ZrO2 nanoparticles stabilized with 10 mol% of ceria using sol-gel (1), microwave (2), and molten salts (3) synthesis.

However, the XRD patterns of MS nanoparticles indicated presence of two ceria-stabilized zirconia phases with different content of ceria. Obviously, the presence of salts in the MS process inhibited interaction of zirconia and ceria. Similar XRD patterns showed zirconia nanoparticles stabilized with 15 mol% ceria. Additional calcination of the as-prepared nanoparticles led to narrowing diffraction maxima of XRD patterns and minimal transformation of tetragonal phase of zirconia to monoclinic (Fig. 3) for nanopowders prepared by MW and MS synthesis indicating the presence of transformable tetragonal zirconia phase in as-prepared particles. The noticeable formation of monoclinic zirconia phase in nanopowders prepared by SG synthesis started at 850 – 900 °C. Content of monoclinic phase of zirconia reached 6 % at calcination temperature 1000 °C.

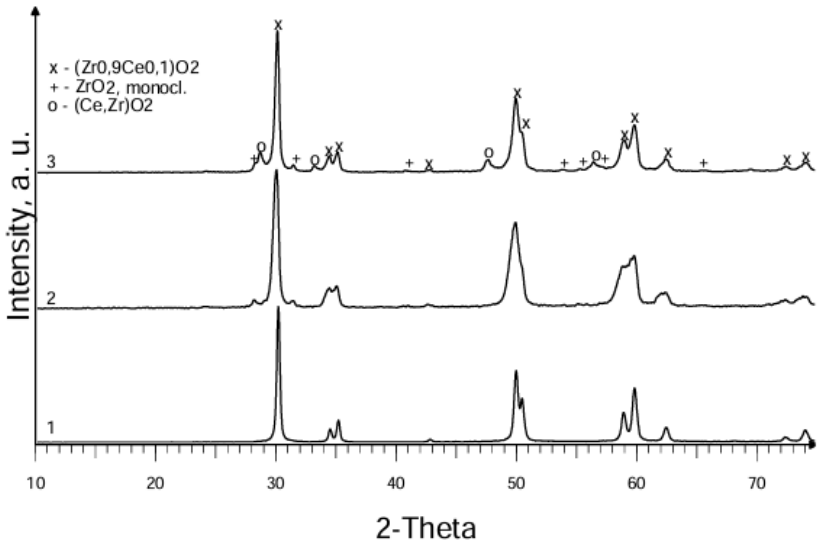

Fig. 3. XRD patterns of calcinated at 800 °C for 2 h stabilized with 10 mol% of ceria using sol-gel (1), microwave (2), and molten salts (3) synthesis

Besides phase composition of the nanoparticles, additional calcination strongly affected the SSA and crystallite size of nanoparticles (Fig. 4).

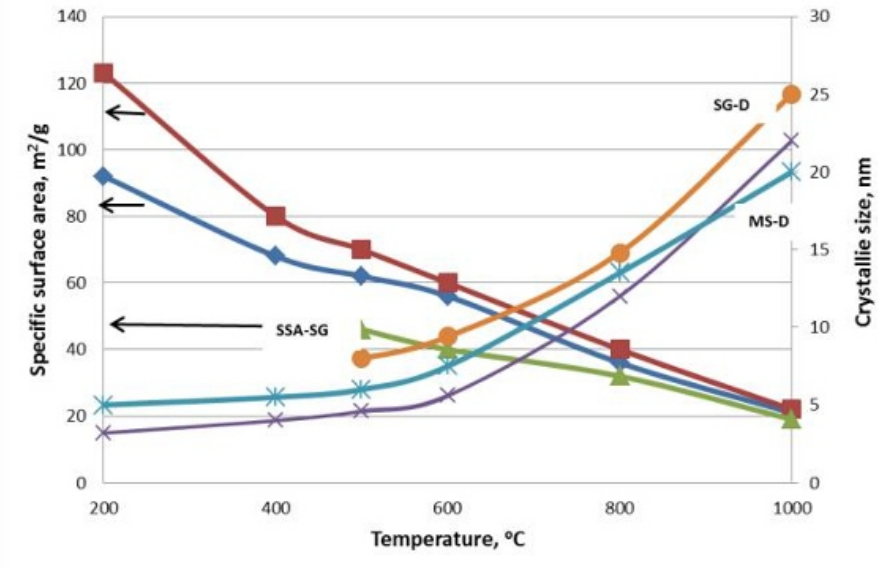

Fig. 4. Dependence of the specific surface area (SSA-MW, SSAMS, SSA-SG) and crystallite size (MW-D, MS-D, SG-D) prepared by MW, MS, SG synthesis on synthesis temperature

Dependence of SSA and crystallite size on calcination temperature was similar for all samples. At temperature of 1000 °C the SSA of all nanoparticles was in the range of 18 – 21 m2/g, and the crystallite size was in the range of 20 – 26 nm; powders prepared by SG synthesis had the higher crystallite size. Using spark plasma sintering densification of well crystalline ceria-stabilized zirconia nanoparticles calcinated at temperature 400 °C, 600 °C and 800 °C started at 850 – 880 °C and final shrinkage was observed at 1260 – 1310 °C (Table 2) depending on the specific surface area and synthesis method.

Table 2. Temperature of shrinkage and relative density of ceria stabilized zirconia samples during SPS process

Synthesis	Calcination temperature, °C	SSA, m^2/g	Temperature of shrinkage, °C		Relative density, %
			starting	final	
MW	400	71.2	860	1280	97.2
MW	800	41.0	870	1290	97.0
MS	400	81.0	850	1300	96.4
MS	800	40.0	880	1310	96.0
SG	600	39.0	850	1260	95.8
SG	800	31.0	860	1280	95.2

Characteristic feature of sintering behavior and density of the samples prepared by each method were dependence of the specific surface area determined by calcination temperature of precursors. However, sintering of the samples prepared by microwave assisted, molten salts and sol-gel combustion method with very close specific surface area – 41.0; 40.0; 39.0 m2/g respectively – showed different density of the bulk materials. Obviously, the sintering was influenced also by different phase composition (Fig. 3) and particle size distribution, degree of agglomeration. The increase of sintering temperature up to 1500 °C and holding time from 3 to 6 min had insignificant influence on the sintering process and density of the samples. The relative density of the samples was in the range of 95.2 – 97.2 % depending on synthesis method and the SSA. The lower density of materials sintered from MS synthesis nanoparticles can be explained by presence solid solution of Zr-Ce-O and reduced content of t-ZrO2 (6 %) due to reduction of oxides [10]. The sintered MW and SG samples contained m-ZrO2 and t-ZrO2 (34 – 42 %) depending on the content of CeO2. The density of SG materials was influenced by the lower specific surface of area of the powders. The microstructure of the sintered bulk materials showed well shaped grains with the size in the range of 0.44 – 1.10 μm (Fig. 5) independently on method of the nanoparticles. The obtained grain size of sintered materials was smaller than that obtained by pressureless sintering of ceriastabilized zirconia at temperature 1400 °C for 2 h (2 μm) prepared by the spray-drying techniques [2]. The relative high grain-size of the manufactured bulk materials despite of low particle size of the precursors could be explained by presence of particle aggregates that accelerated growth of the grains during sintering. Vickers hardness of bulk ceria-stabilized zirconia materials sintered from nanoparticles prepared by MW, MS and SG was 7.8, 6.6, and 7.0 GPa, respectively. The low hardness of material obtained from MS synthesis is related to low density of nanoparticles. From results followed that all applied synthesis methods allowed to prepare ceria stabilized zirconia nanoparticles. However, MS synthesis led to formation of Zr-Ce-O solid solution as extra phase. Presence of this phase influenced sintering final density of materials and reduced strongly content of t-ZrO2.

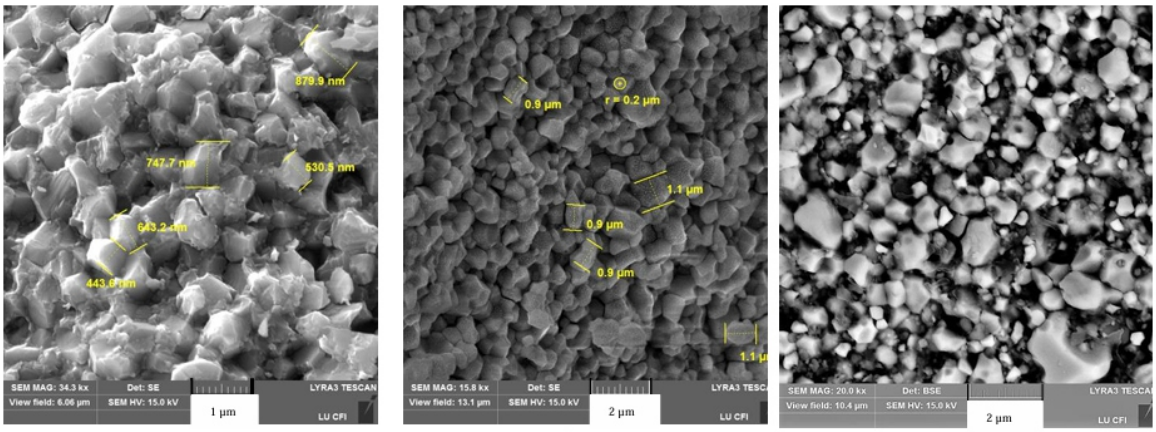

Fig. 5. Fracture surface micrographs of the sintered nanoparticles prepared by: a – MW; b – SG synthesis; c – MS synthesis

Fast spark plasma sintering of MW and SG samples containing t-ZrO2 phase at relatively low temperature limited reduction of oxides [10] and insured good sinterability and density of the bulk materials.

4. CONCLUSIONS

The developed microwave assisted and molten salts synthesis methods allow to prepare ceria-stabilized zirconia nanoparticles with crystallite size in the range of 3.2–5.8 nm what is smaller than that (8.2–9.4 nm) obtained by sol-gel combustion synthesis. Molten salts synthesis promotes formation of cubic solid solution of Zr-Ce-O.

The spark plasma sintering of obtained nanoparticles at 1280–1310 oC allows produce fine-grained materials. Materials obtained from nanoparticles prepared by microwave assisted synthesis have better sinterability and higher density.

The main advantages of the microwave preparation method of ceria-stabilized zirconia are simplicity, low temperature (170–180 oC) and duration (20 min) of the process.

Acknowledgments

The research was supported by State research programme IMIS2.

REFERENCES

1. Lin, J.D., Duh, J.G., Lo, C.L. Mechanical Properties and Resistance to Hydrothermal Aging of Ceria And YttriaDoped Tetragonal Zirconia Ceramics Materials Chemistry and Physics 77 (3) 2003: pp. 808 – 818. https://doi.org/10.1016/S0254-0584(02)00161-X

2. Sharma, S.C., Gokhale, N.M., Dayal, R., Lal, R. Synthesis, Microstructure and Mechanical Properties of Ceria Stabilized Tetragonal Zirconia Prepared by Spray Drying Technique Bulletin of Material Science 25 (1) 2002: pp. 15 – 20. https://doi.org/10.1007/BF02704588

3. Matsuzawa, M., Abe, M., Horibe, S., Sakai, J. The Effect of Reduction on the Mechanical Properties of Ceo2 Doped Tetragonal Zirconia Ceramics Acta Materialia 52 (6) 2004: pp. 1675 – 1682.

4. Cabanas, A., Darr, J.A., Lester, E., Poliakoff, M. Continuous Hydrothermal Synthesis of Inorganic Materials in a Near-Critical Water Flow Reactor; The One-Step Synthesis Of Nano-Particulate Ce1−xZrxO2(x = 0–1) Solid Solutions Journal of Materials Chemistry 11 (2) 2001: pp. 561 – 568. https://doi.org/10.1039/b008095k

5. Rossignol, S., Gerard, F., Duprez, D. Effect of the Preparation Method on the Properties of Zirconia-Ceria Materials Journal of Materials Chemistry 1999: pp. 1615 – 1620. https://doi.org/10.1039/a900536f9

6. Zarkov, A., Stanulis, A., Salkus, T., Kezionis, A., Jasulaitiene, V., Kareiva, A. Ramanauskas, R., Synthesis of Tautkus, S., Nanocrystalline Gadolinium Doped Ceria Via Sol-Gel Combustion and SolGel Synthesis Routes Ceramics International 2016: pp. 3972 – 3988. https://doi.org/10.1016/j.ceramint.2015.11.066

7. 42 Lascalea, G.E., Lamas, D.G., Perez, L., Cabanillas, E.D., Walsoe de Reca, N.E. Synthesis of ZrO2-15 mol% CeO2 Nanopowders by a pH-controlled Nitrate-glycine Process Materials Letters 58 (20) 2004: pp. 2456 – 2460. https://doi.org/10.1016/j.matlet.2004.02.036

8. Zarkov, A., Stanulis, A., Sakaliuniene, J., Butkute, S., Abakeviciene, B., Salkus, T. Tautkus, S., Orliukas, A. F., Tamulevicius, S., Kareiva, A. On the Synthesis of Yttria-stabilized Zirconia: A Comparative Study Journal of Sol-Gel Science and Technology (JSST) 2015: pp. 309 – 319. https://doi.org/10.1007/s10971-015-3778-1 76

9. Bondioli, F., Bonamartini Corradi, A., Ferrari, A.M., Leonelli, C. Synthesis of Zirconia Nanoparticles in a Continuous-Flow Microwave Reactor The Journal of the American Ceramic Society 91 (11) 2008: pp. 3746 – 3748. https://doi.org/10.1111/j.1551-2916.2008.02666.x

10. Xu, T., Wang, P., Fang, P., Kan, Y., Chen, L., Vleugels, J., Van der Briest, Omer., Van Landuyt, J. Phase Assembly and Microstructure of CeO-doped ZrO2 Ceramic Prepared by Spark Plasma Sintering Journal of the European Ceramic Society 25 2005: pp. 3437 – 3442. https://doi.org/10.1016/j.jeurceramsoc.2004.09.004

DFT Study on Electronic Interactions of Pt, Pd and Au Atoms with γ-Al2O3

Han WEI 1, Wenbo DONG 1 , Jianhua CHEN 2, Yuqiong LI 2, Cuihua ZHAO 3

1 Department of Environmental Science and Engineering, Fudan University, Shanghai 200433, China

2 Guangxi Colleges and Universities Key Laboratory of Minerals Engineering, Guangxi University, Nanning 530004, China

3 College of Material Science and Engineering, Guangxi University, Nanning 530004, China

ABSTRACT

The metal-support electronic interaction of dispersed Pt, Pd and Au layers on γ-Al2O3 is studied by density functional theory (DFT) calculations. The results indicate that electrons transfer significantly between the contacting layers of Au, Pt or Pd and the γ-Al2O3. Fukui function calculation results exhibit the electrophilicity of Al and O atoms on the Pt-supported surface is the greatest, while their nucleophilicity is the weakest. DOS calculation results demonstrate that the metal d orbital and O 2p orbital participate in the interactions, and the interaction between Pt 5d orbital and O 2p orbital is the strongest.

Keywords: γ-alumina; noble metal layer; electronic interactions.

INTRODUCTION

γ-alumina (γ-Al2O3) is commonly used as a support in catalysis due to its porousness, high dispersity and large specific surface area. γ-Al2O3 is an activated alumina and has many industrial applications. Transition metals, such as rhodium (Rh), platinum (Pt), and palladium (Pd), can be finely dispersed on this type of ceramic porous support. Many efforts have been made to understand the catalytic activity, spectroscopic properties, and electronic properties of this type of catalyst [1 – 7].

The change of the electronic properties of metal particles after metal-support interaction is very critical for the catalytic activity of materials, and their influence on catalytic properties has garnered considerable attention. The occurrence of electronic effects between metal–support has been established [8 – 11]. Various interaction models have been proposed. Treesukol et al. found that the Pt atom interacts with a Bronsted proton and a nearby framework oxygen, and electrons transferred from the zeolite to the Pt atom, while the Bronsted proton withdrew excess electron density from the Pt atom, causing a zero net charge on the Pt atom [12]. Mallmann et al. [13, 14] proposed that electron transfer between the support oxygen atoms and the nearby metal particles. Using a combination of experimental

measurements and theoretical DFT calculations, Mei et al [3] observed that pentacoordinated Al3+ sites on the γ-Al2O3 (100) surface can inhibit Pt sintering both thermodynamically and kinetically because of their strong interactions with atomic Pt or Pt oxide species. This suggests that the cations on the support may participate in the electronic transfer process. However, Mojet et al [15] proposed that the primary interaction is a Coulomb attraction between the metal particle and support oxygen ions, and this metal–support interaction model does not need electron transfer. These researchers suggested that the decrease in activity of metal clusters with increasing support alkalinity can be ascribed to a decrease in ionization potential of the metal particles directly induced by the Coulomb potential of the support. The metal–support interaction is very important for the use of the catalyst because the desired catalytic reactivity of the supported metal can be obtained if the interaction is well-understood. However, the detailed charge transfer may not be detected by experimental technology due to the effects of the metal particle size and other difficult-tocontrol factors. Gao [16] has performed DFT calculations with the Dmol3 program on the single Pt, Pd, Ag, Sn and In adsorption on the O-terminatedandAl-terminatedγ-Al2O3 (110) surfaces and analysed the adsorption energy, atomic density of states and Mulliken charges. The present study focuses on the electronic interaction between metal layer (Pt, Au and Pd) and γ-Al2O3 support using density functional theory. Based on the calculations, the detailed electronic transfer and interaction can be clearly shown. The results will help to characterize the nature of the metalsupport interaction.

2. COMPUTATIONAL METHODS

In this study, the properties of γ-Al2O3 coated with Au, Pt and Pd metals were studied by density functional theory (DFT) calculations using CASTEP code with GGA-PW91 exchange-correlation potentials. The energy cut off is set to 400 eV and SCF tolerance 1×10-5 eV atom–1. The surface of γ-Al2O3 (101) was cleaved from the optimized bulk state. Vaarkamp et al. have shown that the morphology of the Pt particles was similar to a Pt plane during high temperature reduction, and the Pt–O distance was 2.2 Å on the metalsupport interface [1]. In our study, the metal layer and γAl2O3 layer were built together with a small interval (approximately 2.2 Å) between these two layers, as shown in Fig. 1. In order to eliminate the mirror effect, a vacuum layer was placed at the other end in contrast to the metal/γAl2O3 contact end.

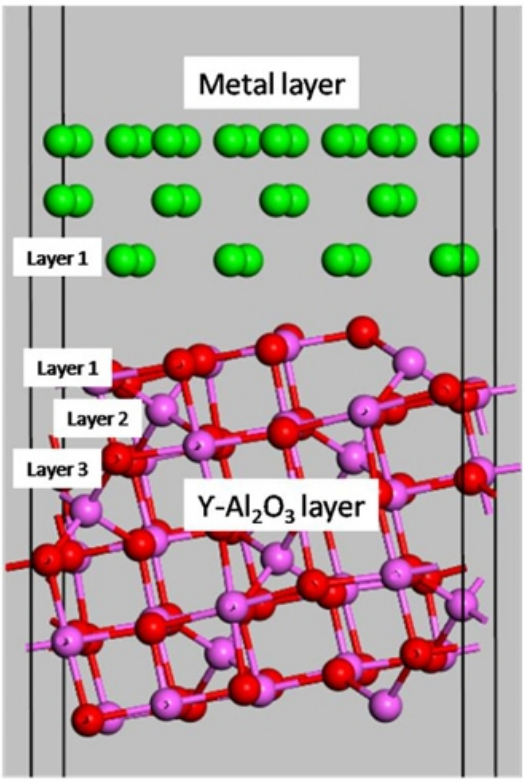

Fig. 1. Calculated model of γ-Al2O3 surface supported metals. The atoms lying on the same plane is labelled as layer 1, layer 2 or layer 3

3. RESULTS AND DISCUSSION

3.1. Charge transfer between metal/γ-Al2O3 interface

The Mulliken charge population of the three layers of Al and O atoms contacting with metals were calculated, and the charges of Al or O atoms on the same layer were added. The results are shown in Table 1. It is shown that the charges of Al or O atoms on layer 1 change significantly after contacting with metals, whereas charges on layer 2 and layer 3 have not changed much. This indicates that Au, Pt and Pd metals have great influence on the charge states of the outer surface atoms of γ-Al2O3. On pure surface, the positive charges of Al atoms are less than the negative charges of O atoms, resulting in the negatively charged outer surface. The positive charge of Al atoms and negative charge of O atoms on the γ-Al2O3 supported Au, Pt and Pd metals decrease compared with that on pure γ-Al2O3. However, the decrease of positive charge of Al atoms is more than the negative charge of O atoms, resulting in the increase of the negative charge of the outer surface. The above results suggest that the interfacial Al takes part in the interaction of metal with support, which is consistent with the study by Mojet et al. [15]. Electron loss of Au, Pt or Pd to the surface was observed. We calculated the total charges of metals on metal layer 1. It is observed that the Pt on metal layer 1 loses the most electrons to the surface, i.e., the Pt atoms on layer 1 have the most positive charges (+1.94 e) followed by Pd (+1.09 e) and Au (+0.55 e).

This finding suggests that the electronic interaction of Pt metal with the γ-Al2O3 surface is the greatest after contact with the surface. It is noted that the outer electronic structures of Au, Pt and Pd are 5d106s1, 5d96s1 and 4d10, respectively. The Pt 5d orbital is not fully filled, while Au 4d and Pd 5d orbitals are fully filled. This finding causes the stronger activity of Pt 5d orbital than either Au 4d or Pd 5d orbitals, and consequently, Pt loses more electrons. In addition, Pd atom has an outer orbital of 6s1, while Au does not have an unfilled s orbital; hence, Pd loses more electrons than Au.

3.2. Electrophilicity and nucleophilicity of surface atoms

It is known that frontier molecular orbital theory (FMO) can be used to predict the chemical reactivity of molecules. Fukui functions (f®) are the analogue of frontier orbitals, both of which are important reactivity criteria [17 – 20]. The function f has different values at different points in the species. It is assumed that the preferred direction is the one with largest f® at the reaction site. Two Fukui indices, f+(r) and f-®, control the nucleophilic attack and electrophilic attack, respectively. The f+® and f (r) are the electrophilic value and nucleophilic value of the r atom, respectively, and the Fukui indices were calculated by Eq. 1 and Eq. 2:

$$f^{+}(r) = \frac{1}{\Delta N}\left(\rho_{N+\Delta}(r) - \rho_{N}(r)\right); \quad (1)$$

$$f^{-}(r) = \frac{1}{\Delta N}\left(\rho_{N}(r) - \rho_{N-\Delta}(r)\right), \quad (2)$$

where the ρ(r) means the charge density of r atom. The r means the atom which was calculated. Moreover, the larger the f+® value, the more susceptible to nucleophilic attack. Similarly, the larger the f (r) value, the more susceptible to electrophilic attack. We calculated the f+® and f-(r) values of surface Al and O atoms, as shown in Table 2. It is found that the Al atom on the γ-Al2O3 surface supported Pt has the largest f+® value followed by that on the surface supported Au and, next, that on the surface supported Pd. The f+® value of O atoms has the same order as Al atom on these three supported metal surfaces. For the f-® index, the Al atom on the surface supported Au is the largest followed by that the surface supported Pd and, next, that on the surface supported Pt. The f-® index of O atom is notably small. There results suggest that the electrophilicity of Al and O atoms on the surface supported Pt is the greatest, while their nucleophilicity is the weakest.

Table 1. Total charges of the three layers atoms contacting with metals (in e)

	Al atoms of layer 1	O atoms of layer 1	Al atoms of layer 2	Al atoms of layer 3	O atoms of layer 3
Pure γ-Al_2O_3	+ 4.80	− 6.62	+ 3.56	+ 7.95	− 11.97
Au/γ-Al_2O_3	+ 3.49	− 5.59	+ 3.33	+ 7.90	− 11.68
Pt/γ-Al_2O_3	+ 3.40	− 5.39	+ 3.31	+ 7.85	− 11.69
Pd/γ-Al_2O_3	+ 3.40	− 5.57	+ 3.26	+ 7.77	− 11.74

Table 2. Fukui indices of surface atoms

	Al		O	
	$f^+(r)$	$f^-(r)$	$f^+(r)$	$f^-(r)$
Au/γ-Al_2O_3	0.013	0.012	0.005	0.004
Pt/γ-Al_2O_3	0.018	0.006	0.011	0
Pd/γ-Al_2O_3	0.011	0.010	0.004	0.004

In addition, it is clearly observed from the specified f+® and f-® values that the nucleophilicity and electrophilicity of Al and O atoms on the surfaces supported Au and Pd are close. Based on the above results, it can be predicted that the Pt-supported γ-Al2O3 surface is the most susceptible to nucleophilic attack. In other words, the electrophilicity of γ-Al2O3 surface supported Pt is the greatest. Hence, the Ptsupported γ-Al2O3 may have a better performance of oxidation of organic matters than Au- and Pd-supported γ-Al2O3.

3.3. DOS of surface atoms

Density of states (DOS) can give clear orbital interactions between atoms and the internal orbital interactions of an atom. Fig. 2 – Fig. 4 show the densities of states (DOSs) of Al, O, and metal atoms, respectively. The Fermi level (EF) is set at zero energy.

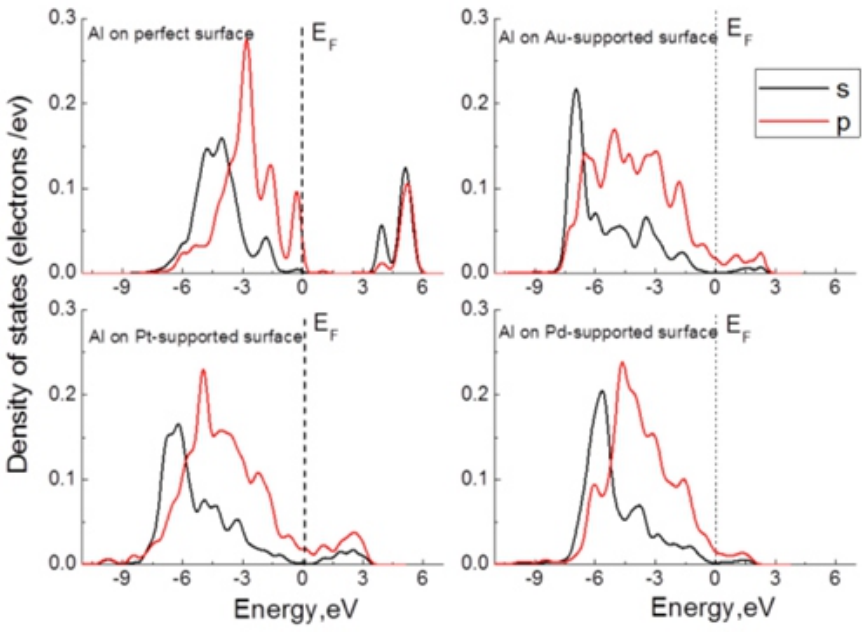

Fig. 2. DOS of Al atoms on pure and metal-coated surfaces

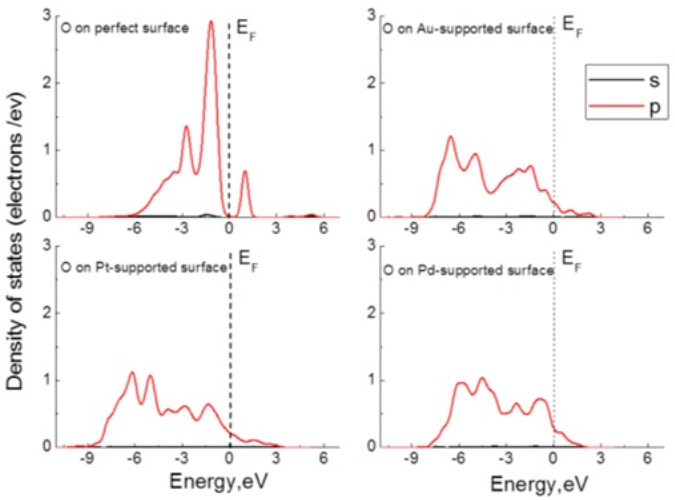

Fig. 3. DOS of O atoms on pure and metal-coated surfaces

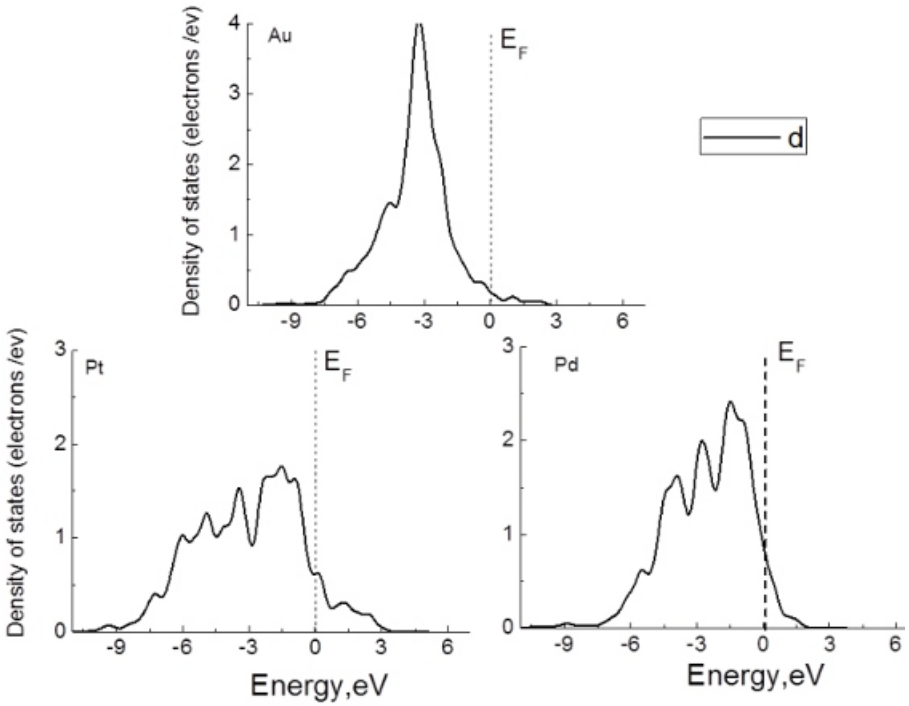

Fig. 4. DOS of metal atoms

It is shown that on pure surface, the valence bands and conduction bands of Al and O atoms are discrete on the two sides of Fermi level. The valence band and conduction band of Al is consisted with 3s and 3p states, and 2p is the main contributor to the DOS of O atom. Although metal interacts with the surface O atom, the DOS of surface Al atom is also significantly influenced. It is found that the 3p orbital of Al atom is continuously connected together across the Fermi level. This situation also occurred for O 2p orbital but not for Al 3s orbital. This suggests that the electronic activity of Al 3p and O 2p orbitals is

enhanced due to the presence of metals. The d orbital of metal is involved in the reaction with O p orbital. It is found that the interaction range between O 2p and Pt d states are the widest (from – 9 to 3 eV). In addition, the width of Al 3p orbital on Pt-supported surface are also the largest (– 10 to 3.5 eV). These results suggest that Al 3p and O 2p electrons on Pt-supported surface have the largest activity compared to the other two metal-supported surfaces This finding indicates that the Pt-supported γ-Al2O3 surface is the most susceptible to nucleophilic attack.

4. CONCLUSIONS

Our theoretical calculations confirm the electronic transfer between Au, Pt or Pd and the γ-Al2O3 interface. Strong electronic interactions occur at the contacting layers of metal and γ-Al2O3 support. It is observed that Al atom obtained electrons after the interaction of metal and O atom, while the metal atom and O atom lost electrons. As per the role of metals, the electrophilicity and nucleophilicity interfacial Al and O atoms are changed. The electrophilicity of Al and O atoms on the Pt-supported surface is the greatest, while their nucleophilicity is the weakest. Furthermore, the nucleophilicity and electrophilicity of Al and O atoms on the surfaces supported Au and Pd are close. Through the calculated results, it is determined that the Ptsupported γ-Al2O3 is the most susceptible to nucleophilic attack, which may have a better performance of oxidation on organic matters in comparison to Au- or Pd-supported γAl2O3. It is found the metal d orbital and O 2p orbital participate in the interactions. Moreover, the interaction between Pt 5d orbital and O 2p orbital is the strongest. The electronic structure of Al 3p is also significantly changed. Only the interface interaction of metal-support was considered in the present study; however, as noted in the introduction, the metal particle size, as well as other difficult-to-control factors, may have great effects on the electronic state of the particle. These aspects warrant further investigation using theoretical calculation methods in future research.

Acknowledgments

The authors would like to acknowledge financial support provided by Guangxi Natural Science Foundation (No. 2014GXNSFAA118342).

REFERENCES

1. Vaarkamp, M., Miller, J.T., Modica, F.S., Koningsberger, D.C. On the Relation Between Particle Morphology, Structure of the Metal-Support Interface, And Catalytic Properties of Pt/γ-Al2O3 Journal of Catalysis 163 (2) 1996: pp. 294 – 305. https://doi.org/10.1006/jcat.1996.0330

2. Srinivasan, A., Depcik, C. Review of Chemical Reactions in the NO Reduction By CO on Rhodium/Alumina Catalysts Catalysis Reviews: Science and Engineering 2010: pp. 462 – 493. https://doi.org/10.1080/01614940.2010.522485

3. Mei, D.H., Kwak, J.H., Hu, J.Z., Cho, S.J., Szanyi, J., Allard, L.F., Peden, C.H.F. Unique Role of Anchoring Penta-coordinated Al3+ Sites in the Sintering of γ-Al2O3Supported Pt Catalysts Journal of Physical Chemistry Letters 1 (18) 2010: pp. 2688 – 2691. https://doi.org/10.1021/jz101073p

4. Koningsberger, D.C., Vaarkamp, M. Influence of the Reduction Temperature on the Structure of the Metal Particles and the Metal-Support Interface of Pt/Γ-Al2O3 Catalysts Physica B Condensed Matter 208 – 209 1995: pp. 633 – 636. https://doi.org/10.1016/0921-4526(94)00776-R

5. Roscioni, O.M., Dyke, J.M. Structural Characterization of Supported RhI(CO)2/γ-Al2O3 Catalysts by Periodic DFT Calculations Journal of Physical Chemistry C 117 (38) 2013: pp. 19464 – 19470. https://doi.org/10.1021/jp405549k

6. Alexeev, O.S., Panjabi, G., Phillips, B.L., Gates, B.C. Carbonylation and Decarbonylation of γ-Al2O3-Supported Hexarhodium Clusters: Characterization by Infrared,13C NMR, and Extended X-ray Absorption Fine Structure Spectroscopies Langmuir 19 (22) 2003: pp. 9494 – 9503. https://doi.org/10.1021/la0348970

7. Fung, A.S., Kelley, M.J., Koningsberger, D.C., Gates, B.C. γ-Al2O3-Supported Re-Pt Cluster Catalyst Prepared from [Re2Pt(CO)12]: Characterization by Extended X-ray Absorption Fine Structure Spectroscopy and Catalysis of Methylcyclohexane Dehydrogenation Journal of the American Chemical Society 1997: pp. 5877 – 5887. 119 (25)

8. Gallezot, P. The State and Catalytic Properties of Platinum and Palladium in Faujasite-Type Zeolites Catalysis ReviewsScience and Engineering 20 1979: pp. 121 – https://doi.org/10.1080/03602457908065108

9. Gallezot, P., Weber, R., Betta, R.A.D., Boudart, M. Cheminform Abstract: Investigation by X-ray Absorption Spectroscopy of Platinum Clusters Supported on Zeolites Chemischer Informationsdienst 34 (14) 1979: pp. 40 – 42. https://doi.org/10.1515/zna-1979-0107

10. Besoukhanova, C., Guidot, J., Barthomeuf, D. Platinumzeolite Interactions in Alkaline L Zeolites. Correlations between Catalytic Activity and Platinum State Journal of Chemical Society-Faraday Transactions 1981: pp. 1595 – 1604.

11. Larsen, G., Haller, G.L. in Pt/L-zeolite Catalysts 1989: pp. 103 – 110. Metal-support Catalysis Letters https://doi.org/10.1007/BF00765061 77 Effects 3 (1)

12. Treesukol, P., Srisuk, K., Limtraku, J., Truong, T.N. Nature of the Metal-support Interaction in Bifunctional Catalytic Pt/H-ZSM-5 Zeolite Journal of Physical Chemistry B 109 (24) 2005: pp. 11940 – 11945. https://doi.org/10.1021/jp0511348

13. Mallmann, A.D., Barthomeuf, D. Correlation between Benzene Hydrogenation Activity and Zeolite Basicity in Ptfaujasites Journal de Chimie Physique et de Physico-Chimie Biologique 87 (4) 1990: pp. 535 – 538.

14. Mallmann, A.D., Barthomeuf, D. Specific Platinum Particles Properties in Basic Zeolites Studies

n Surface Science and Catalysis 46 1989: pp. 429 – 438. https://doi.org/10.1016/S0167-2991(08)60999-4

15. Mojet, B.L., Miller, J.T., Ramaker, D.E., Koningsberger, D.C. A New Model Describing the Metalsupport Interaction in Noble Metal Catalysts Journal of Catalysis 186 (2) 1999: 373 – 386. https://doi.org/10.1006/jcat.1999.2568

16. Gao, H.W. DFT Study of the Absorption Properties of Single Pt, Pd, Ag, In and Sn on the γ-Al2O3(110) Surface Chemical Physics Letters 657 2016: pp. 11 – 17. https://doi.org/10.1016/j.cplett.2016.05.056

17. Parr, R.G., Yang, W. Density Functional Approach to the Frontier-electron Theory of Chemical Reactivity Journal of the American Chemical Society 1984: pp. 4049 – 4050. https://doi.org/10.1021/ja00326a036 106 (14)

18. Ayers, P.W., Levy, M. Perspective on "Density functional Approach to the Frontier-electron Theory of Chemical Reactivity" Theoretical Chemistry Accounts 2000: pp. 353 – 360. https://doi.org/10.1007/s002149900093 103 (3)

19. Geerlings, P., Proft, F.D., Langenaeker, W. Conceptual Density Functional Theory Chemical Reviews 2003: pp 1793 – 1873. https://doi.org/10.1021/cr990029p 103

20. Pintér, B., Proft, F.D., Speybroeck, V.V., Hemelsoet, K., Waroquier, M., Chamorro, E., Veszprémi, T., Geerlings, P. Spin-Polarized Conceptual Density Functional Theory Study of the Regioselectivity in Ring Closures of Radicals Journal of Organic Chemistry 72 2007: pp. 348 – 356. https://doi.org/10.1021/jo0613885

Instructions for Authors

Essentials for Publishing in this Journal

1 Submitted articles should not have been previously published or be currently under consideration for publication elsewhere.

2 Conference papers may only be submitted if the paper has been completely re-written (taken to mean more than 50%) and the author has cleared any necessary permission with the copyright owner if it has been previously copyrighted.

3 All our articles are refereed through a double-blind process.

4 All authors must declare they have read and agreed to the content of the submitted article and must sign a declaration correspond to the originality of the article.

Submission Process

All articles for this journal must be submitted using our online submissions system. http://enrichedpub.com/ . Please use the Submit Your Article link in the Author Service area.

Manuscript Guidelines

The instructions to authors about the article preparation for publication in the Manuscripts are submitted online, through the e-Ur (Electronic editing) system, developed by **Enriched Publications Pvt. Ltd**. The article should contain the abstract with keywords, introduction, body, conclusion, references and the summary in English language (without heading and subheading enumeration). The article length should not exceed 16 pages of A4 paper format.

Title

The title should be informative. It is in both Journal's and author's best interest to use terms suitable. For indexing and word search. If there are no such terms in the title, the author is strongly advised to add a subtitle. The title should be given in English as well. The titles precede the abstract and the summary in an appropriate language.

Letterhead Title

The letterhead title is given at a top of each page for easier identification of article copies in an Electronic form in particular. It contains the author's surname and first name initial .article title, journal title and collation (year, volume, and issue, first and last page). The journal and article titles can be given in a shortened form.

Author's Name

Full name(s) of author(s) should be used. It is advisable to give the middle initial. Names are given in their original form.

Contact Details

The postal address or the e-mail address of the author (usually of the first one if there are more Authors) is given in the footnote at the bottom of the first page.

Type of Articles

Classification of articles is a duty of the editorial staff and is of special importance. Referees and the members of the editorial staff, or section editors, can propose a category, but the editor-in-chief has the sole responsibility for their classification. Journal articles are classified as follows:

Scientific articles:

1. Original scientific paper (giving the previously unpublished results of the author's own research based on management methods).
2. Survey paper (giving an original, detailed and critical view of a research problem or an area to which the author has made a contribution visible through his self-citation);
3. Short or preliminary communication (original management paper of full format but of a smaller extent or of a preliminary character);
4. Scientific critique or forum (discussion on a particular scientific topic, based exclusively on management argumentation) and commentaries. Exceptionally, in particular areas, a scientific paper in the Journal can be in a form of a monograph or a critical edition of scientific data (historical, archival, lexicographic, bibliographic, data survey, etc.) which were unknown or hardly accessible for scientific research.

Professional articles:

1. Professional paper (contribution offering experience useful for improvement of professional practice but not necessarily based on scientific methods);
2. Informative contribution (editorial, commentary, etc.);
3. Review (of a book, software, case study, scientific event, etc.)

Language

The article should be in English. The grammar and style of the article should be of good quality. The systematized text should be without abbreviations (except standard ones). All measurements must be in SI units. The sequence of formulae is denoted in Arabic numerals in parentheses on the right-hand side.

Abstract and Summary

An abstract is a concise informative presentation of the article content for fast and accurate Evaluation of its relevance. It is both in the Editorial Office's and the author's best interest for an abstract to contain terms often used for indexing and article search. The abstract describes the purpose of the study and the methods, outlines the findings and state the conclusions. A 100- to 250-Word abstract should be placed between the title and the keywords with the body text to follow. Besides an abstract are advised to have a summary in English, at the end of the article, after the Reference list. The summary should be structured and long up to 1/10 of the article length (it is more extensive than the abstract).

Keywords

Keywords are terms or phrases showing adequately the article content for indexing and search purposes. They should be allocated heaving in mind widely accepted international sources (index, dictionary or thesaurus), such as the Web of Science keyword list for science in general. The higher their usage frequency is the better. Up to 10 keywords immediately follow the abstract and the summary, in respective languages.

Acknowledgements

The name and the number of the project or programmed within which the article was realized is given in a separate note at the bottom of the first page together with the name of the institution which financially supported the project or programmed.

Tables and Illustrations

All the captions should be in the original language as well as in English, together with the texts in illustrations if possible. Tables are typed in the same style as the text and are denoted by numerals at the top. Photographs and drawings, placed appropriately in the text, should be clear, precise and suitable for reproduction. Drawings should be created in Word or Corel.

Citation in the Text

Citation in the text must be uniform. When citing references in the text, use the reference number set in square brackets from the Reference list at the end of the article.

Footnotes

Footnotes are given at the bottom of the page with the text they refer to. They can contain less relevant details, additional explanations or used sources (e.g. scientific material, manuals). They cannot replace the cited literature.
The article should be accompanied with a cover letter with the information about the author(s): surname, middle initial, first name, and citizen personal number, rank, title, e-mail address, and affiliation address, home address including municipality, phone number in the office and at home (or a mobile phone number). The cover letter should state the type of the article and tell which illustrations are original and which are not.

Note